

SCALINGS AND PLASMA PROFILE PARAMETERISATION OF ASDEX HIGH DENSITY OHMIC DISCHARGES

P.J. Mc Carthy¹, K.S. Riedel², O.J.W.F. Kardaun,
H. Murmann, K. Lackner, the ASDEX Team

Max-Planck-Institut für Plasmaphysik, EURATOM Association,
D-8046 Garching bei München, Fed. Rep. Germany

¹On attachment from University College, Cork, Ireland

²New York University, 251 Mercer St., New York, USA

Abstract

A database of high density ($.3 < \bar{n}_e / 10^{20} \text{m}^{-3} < .8$), low q_a ($1.9 < q_a < 3.4$), Ohmic discharges from the ASDEX experiment is analysed statistically [1]. Bulk parameter scalings and parameterised temperature and density profile shapes are presented. The total plasma kinetic energy, assuming $T_i = T_e$, scales as $\bar{n}_e^{.54 \pm .01} I_p^{.90 \pm .04}$ and is almost independent of B_t . The electron temperature profile peaking factor scales as $T_0^{3/2} / \langle T^{3/2} \rangle = .94 (\pm .04) q_a^{1.07 \pm .04}$ in close agreement with the assumption of classical resistive equilibrium. In the inner half of the plasma, the inverse fall-off length for both temperature and density has a strong dependence on q_a , with the temperature dependence being more pronounced. Outside the half radius, the q_a dependence disappears but the density profile broadens near the edge with increasing plasma current. A second database of moderate density, moderate q_a discharges ($.2 < \bar{n}_e / 10^{20} \text{m}^{-3} < .4$, $2.4 < q_a < 4.2$), is presented for comparison.

1. INTRODUCTION

In most high magnetic field tokamaks, the experimental Ohmic energy confinement time increases roughly linearly with plasma density over a large range of densities. In general, moderate field devices observe a similar but weaker increase in confinement time at small to moderate densities. Unfortunately, the Ohmic energy confinement time saturates at higher values of the Murakami parameter $\bar{n}_e R/B_t$ [2]. This phenomenon is termed density rollover and, under usual operating conditions in ASDEX, occurs at line-averaged densities around $.25 \times 10^{20} \text{m}^{-3}$ and magnetic fields on the order of two Tesla. (Pellet fuelled discharges and the recently discovered Improved Ohmic Confinement regime on ASDEX [3] are not considered here.) We present a statistical analysis of the bulk parameter scalings and profile shapes in this saturated high density regime. For a detailed discussion of the theoretical aspects of profile shape determination, the reader is referred to [1], which we abbreviate as KRML.

In our datasets, neither of which extends into the linear regime, no significant change was observed in the scaling of the total kinetic plasma energy as the rollover density was crossed and exceeded. Plasma energy and the Ohmic power scalings nearly cancel, leaving a moderate q_a dependence ($\tau_E \sim q_a^3$) in the confinement time.

To analyse the profile shapes, we fit all the measured profiles simultaneously by means of a radial spline function each of whose coefficients depends on the plasma parameters q_a , I_p and \bar{n}_e . This powerful technique enables us to quantify the various parametric dependencies as a function of radius. For the electron temperature profile, we find that the profile shape variation consists almost exclusively of a q_a dependence confined to $r/a \leq .60$. The density profile also exhibits a q_a dependence, though it is weaker than that of the temperature. Unlike the temperature, however, we find a broadening of the density profile near the plasma edge with increasing plasma current.

Our research systematises and validates earlier graphical and qualitative studies of “profile consistency”. (See [4] for a review of this topic.) The statistical approach enables us to make quantitative statements about the relative

strength of the interior q_a dependence and the weaker exterior parametric dependencies of the profile shape.

Previous authors have reported a variety of different results on the peaking factor and the interior domain scalings. The multiplicity of results arises from a combination of tokamak to tokamak differences, different physics regimes, systematic measurement errors, and sometimes also from the use of relatively unsophisticated analysis methods. We find, for instance, that normalising by $\langle T^{3/2} \rangle^{2/3}$ in the temperature profile peaking factor calculation removes the ambiguities associated with $\langle T \rangle$ and we obtain a scaling closely consistent with the assumption of resistive equilibrium between temperature and current density. Using the result that the (inverse) fall-off length is solely dependent on q_a , we show that the temperature profile shape cannot be Gaussian.

In Sec. 2, we describe our low q_a , high density and moderate q_a , moderate density databases. In Sec. 3, bulk plasma parameter regressions are presented, including new results for the Wp and Z_{eff} scalings. In Sec. 4, peaking factors and central temperature scalings are examined. Sec. 5 summarises the spline model and the statistical methods used in the profile analysis. Sec. 6 discusses a number of practical techniques to improve the analysis. One of these is to separate the parameterisation of the profile shape and size. Sec. 7 presents our experimental shape analysis results in detail. A discussion and summary is made in Sec. 8. In the appendix, we discuss the statistical significance of each regression variable in a least squares regression model. We note that Secs. 5 and 6 and the appendix may be omitted by those readers who are interested only in the results and not the statistical methods.

2 DATABASE DESCRIPTION

The main (high density) database consists of 105 pairs of time-compressed experimental electron temperature and density profiles from 50 ASDEX deuterium discharges with a corresponding set of bulk plasma parameters and equilibrium flux surface information. Each compressed profile typically consists of the time average of 12 consecutive ‘raw’ profiles sampled at 17 msec

intervals using the ASDEX Nd:YAG ('YAG') Thomson scattering system [5]. All profiles are measured during the current flat-top Ohmic phase of the discharge. Apart from making the data analysis more manageable, the preliminary compression had the effect of strongly reducing profile fluctuations due to sawteeth. Such averaging is free from bias as long as the sawtooth period ($\simeq 10\text{msec}$) is incommensurate with the sampling period. Some typical parameter values for this database are the line-averaged electron density $\bar{n}_e = .4 \times 10^{20}\text{m}^{-3}$, the plasma current $I_p = 400\text{kA}$, and the cylindrical edge $q_a = 2.5$. ASDEX discharges have a fixed circular geometry with $R_{plasma} = 1.65\text{m}$ and $a_{minor} = .40\text{m}$. Table I(a) presents a more detailed summary of the database. All datapoints consist of double-null divertor discharges in deuterium from three consecutive shot days (404 to 406) spanning a one week period in February 1986 during which titanium gettering was extensively used (about every third discharge). One of the experimental goals for these shot days was a density limit investigation, resulting in the presence of a density ramp of .2 to $.4 \times 10^{20}\text{m}^{-3}\text{s}^{-1}$ for 10 out the 50 discharges, which accounted for $\simeq 50\%$ of the datapoints. For the affected discharges, this implies a typical density variation about the mean of $\pm 7\%$ for each 200 msec time window. In selecting the discharges, care was taken to cover as wide a range in ASDEX control parameter operating space as possible. The main toroidal field is relatively seldom varied, however, and two thirds of the datapoints are clustered at toroidal magnetic field values of 1.8T or 2.2T. Nevertheless, the distinction between q_a , B_t and I_p scaling will be quite apparent. Bolometric measurements showed that radiation losses for these discharges ($10\% < P_{rad}/P_{Ohmic} < 40\%$, increasing with density) were strongly localised at the plasma edge.

For comparison, we present a complementary analysis of a second database (38 compressed datapoints from 38 deuterium discharges) of moderate density ($\bar{n}_e \simeq .3 \times 10^{20}\text{m}^{-3}$), moderate q_a ($q_a \simeq 3.1$), non-gettered, Ohmic discharges which is summarised in Table I(b). On ASDEX, these densities are centred around the transition to the rollover regime. These discharges were made over a six month period spanning 64 shot days from August 1985 to February 1986 and were selected from days where the vacuum vessel was

in a nominally normal state (no gettering, stainless steel walls). At other times within this period, however, the experiment was run under a variety of conditions including carbonised walls and three days of operating with He as working gas. In addition, the vessel was open for several weeks in December 1985. The YAG system was calibrated using Raman scattering from hydrogen gas on two occasions during this period. Our database contains no data quantifying the resulting changes or residual effects of these operating periods on the wall condition and, in particular, the condition of the YAG diagnostic window itself. Hence we expect the residual error to the fits to these experimental data to be larger. For these reasons, we include the scalings of the second database largely for purposes of comparison. The distribution of datapoints for each dataset is displayed in the combined Hugill plot (Fig. 1).

The two databases differ in three parameters, \bar{n}_e , q_a , and wall condition (gettered / non-gettered). Thus we can view the combined database as being clustered in two cells of eight possible combinations. Indeed, some scaling differences between the two sets of data were visually apparent in preliminary efforts at fitting the combined dataset. By analysing each database separately, we are able to estimate secondary, weaker effects that are not immediately apparent in a joint analysis. In our case, these effects are weak current and density dependencies of the outer section of the normalised density profiles. If the two data sets were combined, these weaker effects would be obscured by artificial secondary scalings arising from the clustering mentioned above.

As is typical of single machine databases, geometric parameters such as the plasma position and cross-sectional area vary very little (about 1%) and, once the channel positions have been mapped onto the normalised flux surface coordinate ($0 \leq r \leq 1$), these variables are ignored in the analysis. We assume that the macroscopic plasma state is essentially determined by the line-averaged density \bar{n}_e and two of the three parameters I_p , q_a and B_t . These parameters represent the major control parameters which the experimentalist utilises to vary the plasma state in an Ohmic plasma.

The condition of the plasma wall may significantly influence plasma performance. In an effort to include these effects, an additional plasma variable

such as the effective ion charge Z_{eff} , or the total Ohmic power P_{Ω} is sometimes used as an extra independent variable. Both Z_{eff} and P_{Ω} depend on the control parameters \bar{n}_e , I_p and q_a , and therefore are not purely measures of the condition of the plasma wall.

To examine the extent to which the Ohmic power and Z_{eff} vary independently of the control parameters \bar{n}_e , I_p and q_a , we carry out a principal component analysis (PCA) [6]: The correlation matrix of the logarithms of \bar{n}_e , I_p , q_a , Z_{eff} , and P_{Ω} is calculated and diagonalised (see Table II). Each eigenvalue is interpreted as the sample variance of the corresponding principal component over the database, and a small eigenvalue indicates a near collinearity between the original variables. Since the principal components, by construction, are statistically uncorrelated, the sum of a subset of eigenvalues gives the cumulative variance explained by the corresponding subset of principal components. We find that, for both databases, *over 97% of the (standardised) data variation can be explained by the first three components.* The residual 3% of the total variance is attributed to noise in the temperature measurements which affects Z_{eff} and noise in U_{loop} which affects both Z_{eff} and P_{Ω} . Hence, we discard the principal components having the two smallest eigenvalues.

The remaining eigenvectors span a three-dimensional subspace. This subspace can be efficiently represented by linear combinations of any well-conditioned set of three of the five variables. That \bar{n}_e , I_p and q_a constitute such a well-conditioned set is checked by re-doing the PCA for these three alone. The eigenvalues of the 3×3 correlation matrix, also listed in Table II, are all of the same order of magnitude, indicating that, unlike the larger set, no near collinearity exists between them.

For scalings of the bulk parameters, we generally preferred to use the logarithms of \bar{n}_e , B_t , and I_p because the correlation between I_p and B_t was much less than that of either variable with q_a (see Table II(c)). However, some scalings are given in terms of \bar{n}_e , q_a and BI , where the latter parameter was chosen to maintain a set of nearly uncorrelated bulk variables. The dominance of q_a and the weak I_p influence in determining plasma profile shapes motivated us to use \bar{n}_e , I_p and q_a for the profile shape analysis.

3 BULK SCALINGS

In this section, we examine the scalings of the bulk plasma variables. Let us briefly summarise our results: The scaling of the total plasma energy as determined by kinetic measurements is virtually the same in both databases, i.e. no transition was observed going from the rollover to the saturated Ohmic confinement (SOC) regime. However, the diamagnetic and equilibrium mhd estimates of this parameter show strong differences between the two databases. The plasma energy and the Ohmic heating power have roughly similar parametric dependencies, which results in a confinement time scaling consisting mainly of a rather moderate q_a dependence. Power law scalings for Z_{eff} as well as for $Z_{eff} - 1$ are also presented. The latter parameter scales like $1/\bar{n}_e$, indicating that the impurity density is independent of \bar{n}_e .

We use the Spitzer value for the effective ion charge Z_{eff} , which is calculated from the electron temperature profile assuming resistive equilibrium (well satisfied for the current flat-top profiles selected) and Spitzer conductivity. We note that it cannot be used as an independent parameter in the temperature profile regressions below. Recent Bremsstrahlung measurements on ASDEX [7] show that for the SOC regime (to which our high density database belongs), Z_{eff} is very flat over most of the plasma radius, though tending to rise strongly near the boundary. We adopt the conventional assumption of zero radial dependence here. The ion density is calculated with the assumption that the sole impurity is oxygen. The plasma kinetic energy, $W_{Pkin} = \frac{3}{2} \int (n_e T_e + n_i T_i) dv$, is calculated by assuming the ion temperature is equal to the electron temperature, $T_i = T_e$. This assumption is justified when the electron-ion energy exchange time is much shorter than the energy confinement time. In the main database, the typical values are $\tau_{ei} = 5$ msec and $\tau_E = 75$ msec. In some of the moderate density discharges, this condition is not satisfied.

As an independent measure of the plasma energy content we also make use of the diamagnetic flux measurement on ASDEX whose interpretation is not affected by the uncertainty in T_i and is further simplified, in the case of Ohmic plasmas, by the absence of pressure anisotropy. The extreme sensitivity of the

measurement ($\frac{\psi_{dia}}{\psi_{tor}} \simeq 10^{-4}$) to such factors as slight mechanical displacements of the diamagnetic loop means, however, that the typical error associated with the derived value for beta poloidal is $\delta(\beta_{p(dia)}) = \pm .05$. For $\beta_{p(dia)} \simeq 0.3$ (the lower limit in each database) this implies an error of some $\pm 15\%$ in the diamagnetic energy and confinement time. For these databases, the diamagnetic energy is systematically greater than the kinetic energy with an energy-independent offset $\simeq 6 \pm 2$ kJ (see Fig. 2).

A third measure of the plasma energy is derived from equilibrium magnetic measurements, from which the parameter $\beta_{pol} + l_i/2$ can be recovered. To isolate β_{pol} , we need an estimate for $l_i/2$, which, as is well known, cannot be determined from equilibrium data in the case of circular plasmas. From an earlier investigation, we use the following empirical relation from a parameterisation of current density profiles derived from experimental temperature profiles and the assumption of Spitzer resistive equilibrium: $l_i/2 = .332 + .199 \ln q_a$.

The regression models considered are of the form $y = \sum_i \alpha_i x_i + \epsilon$ where y and x denote the logarithms of the dependent and independent bulk plasma variables respectively. The root mean square error (RMSE) of the fit is $\sqrt{\sum_{i=1}^N (y_i - \hat{y}_i)^2 / (N - p)}$ where p is the number of independent variables (including the intercept) and \hat{y}_i is the fitted value of y_i . As our response variables are natural logarithms, the RMSE corresponds to a relative error in the physical variable. We also quote the squared multiple correlation coefficient R^2 , which represents the fraction of total variance about the mean accounted for by the fit: $R^2 = \sum_i (\hat{y}_i - \bar{y})^2 / \sum_i (y_i - \bar{y})^2$. In the bulk scaling results that follow, all physical variables are expressed in the units of Table I.

Total Plasma Energy Scaling

The plasma energy content from kinetic data for the main database satisfies

$$W_{P_{kin}} = 133(\pm 6) \bar{n}_e^{.54 \pm .01} I_p^{.90 \pm .04} B_t^{.06 \pm .04} \quad \text{RMSE} = .04 \quad R^2 = .965$$

Similarly, the scaling law based on the secondary database is

$$W_{P_{kin}} = 128(\pm 6) \bar{n}_e^{.53 \pm .03} I_p^{.80 \pm .05} B_t^{.13 \pm .05} \quad \text{RMSE} = .04 \quad R^2 = .959$$

The plasma energy content inferred from the diamagnetic flux for the main

database is described by

$$\text{Wp}_{dia} = 130(\pm 6)\overline{n_e}^{.40\pm.01} I_p^{.88\pm.04} B_t^{.13\pm.04} \quad \text{RMSE} = .04 \quad \text{R}^2 = .943$$

whereas the secondary database gave a poorer fit:

$$\text{Wp}_{dia} = 83(\pm 10)\overline{n_e}^{.21\pm.05} I_p^{.77\pm.07} B_t^{.33\pm.08} \quad \text{RMSE} = .06 \quad \text{R}^2 = .878$$

The plasma energy content derived from equilibrium magnetic measurements for the main database is described by

$$\text{Wp}_{mhd} = 156(\pm 5)\overline{n_e}^{.41\pm.01} I_p^{.94\pm.03} B_t^{-.01\pm.03} \quad \text{RMSE} = .03 \quad \text{R}^2 = .968$$

whereas the secondary database gave

$$\text{Wp}_{mhd} = 255(\pm 28)\overline{n_e}^{.26\pm.04} I_p^{1.19\pm.06} B_t^{-.36\pm.07} \quad \text{RMSE} = .05 \quad \text{R}^2 = .940$$

The criterion for ‘significance’ of a regressor is whether or not the regression coefficient is at least twice its standard deviation. In the appendix, the statistical background of this simple rule and its relation with R^2 is discussed.

From the indicated uncertainties (1 standard deviation) of the regression coefficients, we see, for instance, that the B_t scaling for Wp_{kin} is insignificant for the main database, while in the secondary database it is (just about) statistically significant. In both cases, omission of B_t affects the goodness of fit only slightly in absolute terms (eq. (A7) gives $\Delta(\text{R}^2) \simeq .001, .007$ respectively).

Because of the design of the database, the correlations between n_e , I_p and B_t are small (see Table II(c)). This results in small correlations between the regression estimates of the exponents of n_e , I_p and B_t . In our regressions, all these correlations are less than 0.15 for the main and less than 0.35 for the secondary database. For assessing the significance of the difference between a postulated scaling law and our empirical scalings, such low correlations between the estimates can be neglected in practice.

The toroidal field shows the most extreme variation in the six Wp scalings presented above. There is also, however, a strong tendency for the I_p coefficient to move in the opposite direction to B_t when going from one scaling to another. This suggests a representation with q_a . To preserve the near independence of the regression estimates, we choose BI as the conjugate variable [8]. In the new representation, we have the following regression coefficients for the six cases (same order as above)

$$B_t I_p : (.49, \quad .46, \quad .52, \quad .55, \quad .48, \quad .42),$$

$$q_a : (-.42, \quad -.32, \quad -.37, \quad -.20, \quad -.47, \quad -.75).$$

The errors in the coefficients are roughly the same as in the (I_p, B_t) scaling. Obviously, to a good approximation, the simple transformation $\alpha_{BI} = \frac{1}{2}(\alpha_B + \alpha_I)$ and $\alpha_q = \frac{1}{2}(\alpha_B - \alpha_I)$ holds. We roughly summarise: $Wp \simeq (BI)^{0.5 \pm 0.05} q_a^{-0.5 \pm 0.25}$, where here the approximate *ranges* are indicated for the regression coefficients in the six cases above. Hence, at constant \bar{n}_e , the BI scaling is nearly constant, but the q_a scaling varies considerably with the type of measurement and with the database.

The reasons for the observed q_a scaling differences may be partly due to physics, and partly to systematic errors. Wp_{mhd} is particularly vulnerable to errors in the $\simeq 50\%$ $l_i/2$ correction to $\beta_{pol} + l_i/2$. To get an idea of the influence of this error, we performed a sensitivity analysis. Using $l_i/2 = .332 + \delta_1 + (.199 + \delta_2) \ln q_a$, we made a number of Wp_{mhd} regressions for different choices of δ_1 and δ_2 in the range $-.1$ to $+1$. (Note that δ_1 can describe an error in $\beta_{pol} + l_i/2$ as well as in $l_i/2$.) We found that the exponent for q_a in the Wp_{mhd} regression varied as $-.47 + 1.3\delta_1 - 1.6\delta_2$ for the main database and $-.75 + .43\delta_1 - 2.0\delta_2$ for the secondary database. Thus an error of $-.1$ in the $\ln q_a$ coefficient for $l_i/2$ (we would expect this to be an extreme case) gives q_a exponents of $-.31$ and $-.55$ for main and secondary databases respectively. We conclude that this error source cannot reconcile the scaling of Wp_{mhd} with q_a for the secondary database with the remaining five Wp scalings.

Now we turn to Wp_{dia} . Suppose we have an offset δ_β in $\beta_{pol,dia}$. A sensitivity analysis showed that this roughly gives an offset of $-2\delta_\beta$ in the q_a coefficient (for both data bases). The density dependence is offset by $-\delta_\beta$ for the main data base and by $-0.5\delta_\beta$ for the secondary database. It is noted that the observed $6kJ$ systematic difference between the Wp_{kin} and Wp_{dia} measurements corresponds (at $I_p = .4$ MA) to a difference in β_{pol} of 0.05 , which is consistent with the observed difference in q_a dependence between Wp_{kin} and Wp_{dia} for either database. Similarly, it explains half of the difference in n_e dependence. It does not, however, offer a satisfactory explanation for the Wp_{dia} or Wp_{mhd} scaling differences *between* the databases, for which we must appeal to the already referred to differences in operating regimes

(gettered/non-gettered walls, high densities/rollover densities, etc.).

Volume Averaged Electron Temperature

Both databases are in rough agreement with the Pfeiffer-Waltz [9] and JET Ohmic scalings [10]. The main database satisfies

$$\langle T_e \rangle = 0.639(\pm 0.03)\bar{n}_e^{-.52\pm.01} I_p^{.97\pm.04} B_t^{-.04\pm.04} \quad \text{RMSE} = .04 \quad R^2 = .947$$

Similarly, the secondary database satisfies

$$\langle T_e \rangle = 0.605(\pm 0.06)\bar{n}_e^{-.61\pm.04} I_p^{.93\pm.06} B_t^{.04\pm.07} \quad \text{RMSE} = .05 \quad R^2 = .913$$

Here, B_t is insignificant for both databases and its omission has a very small ($\simeq .001$) effect on R^2 . Though a natural candidate for determining the temperature, we have not included Z_{eff} in the list of regressors, since, in our case, it is derived, assuming Spitzer resistivity, from the temperature profile itself:

$$Z_{eff} \propto \frac{\langle T^{\frac{3}{2}} \rangle_{area} V_{loop}}{I_p R_{plas}}$$

(neglecting variations in the Coulomb logarithm).

Loop Voltage/Ohmic Power

We present the loop voltage scalings. The Ohmic power scalings differ from these by exactly one power of I_p . For the main database, the loop voltage scales as

$$V_{loop} = 2.38(\pm 0.1)\bar{n}_e^{.36\pm.02} I_p^{.12\pm.05} B_t^{-.27\pm.04} \quad \text{RMSE} = .04 \quad R^2 = .864$$

Similarly, the secondary database satisfies

$$V_{loop} = 2.40(\pm 0.1)\bar{n}_e^{.30\pm.02} I_p^{.19\pm.03} B_t^{-.31\pm.03} \quad \text{RMSE} = .03 \quad R^2 = .896$$

Due to the additional factor of I_p on both sides, we get necessarily higher R^2 values (.935 and .984) for the Ohmic power regressions (The RMSE values are unchanged).

Spitzer Z effective

For the main database, the Spitzer Z_{eff} scales as

$$Z_{eff} = 2.90(\pm 0.18)\bar{n}_e^{-.48\pm.02} I_p^{.67\pm.05} B_t^{-.34\pm.05} \quad \text{RMSE} = 0.05 \quad R^2 = .893$$

Regressing the impurity contribution to Z_{eff} gives an entirely different scaling:

$$Z_{eff} - 1 = 2.21(\pm 0.33)\bar{n}_e^{-1.14 \pm 0.04} I_p^{1.51 \pm 0.12} B_t^{-.81 \pm 0.12} \quad \text{RMSE} = .18 \quad R^2 = .844$$

For moderate densities, the Spitzer Z_{eff} scales as

$$Z_{eff} = 2.67(\pm 0.58)\bar{n}_e^{-.69 \pm 0.08} I_p^{.64 \pm 0.11} B_t^{-.22 \pm 0.13} \quad \text{RMSE} = .09 \quad R^2 = .714$$

The impurity scaling yielded

$$Z_{eff} - 1 = 1.83(\pm 0.71)\bar{n}_e^{-1.10 \pm 0.14} I_p^{1.07 \pm 0.19} B_t^{-.43 \pm 0.21} \quad \text{RMSE} = .16 \quad R^2 = .709$$

Using the relation $n_{H;D} = n_e - \sum_i n_i Z_i$ (i-summation over impurity species only), $Z_{eff} \equiv \sum_j n_j Z_j^2 / n_e$ (j-summation over all species) can be re-expressed as

$$Z_{eff} = 1 + \frac{\sum_i n_i (Z_i^2 - Z_i)}{n_e}$$

With this representation, we see that *the \bar{n}_e exponents in the impurity scalings suggest an impurity density (almost) independent of the line density.* The strong I_p and B_t scalings are not so readily interpretable.

Energy Confinement Time

The I_p and \bar{n}_e dependencies of the total plasma energy and the Ohmic power approximately cancel to leave a relatively weak q_a dependence in τ_E . This makes the energy confinement scalings less pronounced. The main database yielded the following scaling for the kinetic τ_E :

$$\tau_{Ekin} = 56(\pm 5)\bar{n}_e^{.18 \pm 0.03} I_p^{-.21 \pm 0.08} B_t^{.34 \pm 0.08} \quad \text{RMSE} = .07 \quad R^2 = .392$$

The secondary database fit yielded

$$\tau_{Ekin} = 53(\pm 6)\bar{n}_e^{.23 \pm 0.05} I_p^{-.39 \pm 0.06} B_t^{.44 \pm 0.07} \quad \text{RMSE} = .05 \quad R^2 = .709$$

As explained in the discussion of the Wp scaling, we prefer the representation in terms of $B_t I_p$ and q_a :

$$\tau_{Ekin} = 68(\pm 4)\bar{n}_e^{.18 \pm 0.03} (BI)^{.06 \pm 0.06} q_a^{.28 \pm 0.05} \quad (\text{High density database})$$

$$\tau_{Ekin} = 72(\pm 6)\bar{n}_e^{.22 \pm 0.05} (BI)^{.02 \pm 0.04} q_a^{.41 \pm 0.05} \quad (\text{Moderate density database})$$

The confinement time derived from the diamagnetic measurement of the energy content for the main database scales as

$$\tau_{Edia} = 69(\pm 3)\bar{n}_e^{.04 \pm 0.02} (BI)^{.08 \pm 0.05} q_a^{.33 \pm 0.04} \quad \text{RMSE} = .06 \quad R^2 = .403$$

The secondary database fit yielded

$$\tau_{Edia} = 50(\pm 5)\bar{n}_e^{-.10 \pm 0.05} (BI)^{.11 \pm 0.05} q_a^{.53 \pm 0.06} \quad \text{RMSE} = .06 \quad R^2 = .699$$

The confinement time derived from equilibrium magnetic measurements for the main database scales as

$$\tau_{Emhd} = 77(\pm 3)\bar{n}_e^{.04\pm.02}(BI)^{.04\pm.04}q_a^{.23\pm.04} \quad \text{RMSE} = .06 \quad R^2 = .260$$

The secondary database fit yielded

$$\tau_{Emhd} = 103(\pm 9)\bar{n}_e^{-.04\pm.05}(BI)^{-.03\pm.05}q_a^{-.02\pm.06} \quad \text{RMSE} = .06 \quad R^2 = .036$$

The difference in q_a scaling between the two databases suggests the possibility of a quadratic (i.e. $\ln q_a \ln q_a$) dependence [8]. No curvature in the $\ln q_a$ dependence was apparent, however, in a plot of $\ln \tau_{Edia}$ for both databases with their respective \bar{n}_e and BI dependencies removed. Fig. 3 shows $\ln \tau_{Edia}/(BI/.8)^{.08}(\bar{n}_e/.4)^{.04}$ for the main database and $\ln \tau_{Edia}/(BI/.8)^{.11}(\bar{n}_e/.4)^{-.10}$ for the secondary database. A similar picture holds for $\ln \tau_{Ekin}$, whereas for $\ln \tau_{Emhd}$ there appeared to be a deterioration at high q_a (figures not shown). Three points at low q_a seem to be somewhat outlying in Fig. 3. However, their removal does not change the $\ln q_a$ regression coefficient by more than one standard deviation. Unlike some previous reported results (see, e.g., [13] section 4) we found *no significant confinement time deterioration with density in the SOC regime*. Fig. 4 shows τ_{Ekin} (with I_p and B_t dependencies removed) versus \bar{n}_e for both databases, i.e. $\ln \tau_{Ekin}/(I_p/.4)^{-.21}(B_t/2)^{.34}$ for the main database and $\ln \tau_{Ekin}/(I_p/.4)^{-.39}(B_t/2)^{.44}$ for the secondary database. Similar behaviour is observed for both τ_{Edia} and τ_{Emhd} . For the difference in q_a scaling, the reader is referred to the sensitivity discussion in the subsection on total plasma energy.

4. CENTRAL TEMPERATURE AND PEAKING FACTORS

4.1 Electron Temperature, Density and Pressure at $r = 0.2$

To enable reconstruction of absolute profiles from the profile shape scalings presented later, we regressed T_e , n_e and $p_e = 1.5n_eT_e$ at the 20% flux radius. This normalisation radius lies inside the inversion radius for our q_a range and also has data points on either side of it. (The YAG channel closest to the magnetic axis lies typically on the 14% flux radius.) The high density low q_a database satisfies

$$T_e \text{ 20\%} = .369(\pm.02)\bar{n}_e^{-.49\pm.01} I_p^{.29\pm.04} B_t^{.71\pm.04} \quad \text{RMSE} = .04 \quad R_2 = .937$$

$$n_e \text{ 20\%} = .802(\pm.01)\bar{n}_e^{.98\pm.01} I_p^{-.28\pm.02} B_t^{.21\pm.02} \quad \text{RMSE} = .02 \quad R_2 = .997$$

$$p_e \text{ 20\%} = .444(\pm.02)\bar{n}_e^{.49\pm.02} I_p^{.01\pm.05} B_t^{.92\pm.05} \quad \text{RMSE} = .05 \quad R_2 = .925$$

while the secondary database yielded

$$T_e \text{ 20\%} = .404(\pm.04)\bar{n}_e^{-.58\pm.05} I_p^{.31\pm.06} B_t^{.71\pm.07} \quad \text{RMSE} = .05 \quad R_2 = .879$$

$$n_e \text{ 20\%} = .922(\pm.05)\bar{n}_e^{1.05\pm.02} I_p^{-.34\pm.03} B_t^{.13\pm.04} \quad \text{RMSE} = .03 \quad R_2 = .984$$

$$p_e \text{ 20\%} = .560(\pm.07)\bar{n}_e^{.47\pm.06} I_p^{-.03\pm.08} B_t^{.84\pm.09} \quad \text{RMSE} = .06 \quad R_2 = .864$$

Most noteworthy here is the $\sqrt{\bar{n}_e} B_t$ - like dependence of $p_e \text{ 20\%}$ for both databases. On regressing p_e at each of the five most central YAG channels, which typically lie between the 14% and 25% flux radii, we found a similar absence of an I_p dependence (coefficients ranged from 0. to .05 with a typical standard deviation of .05 for the main database; -.13 to .18 with a typical standard deviation of .075 for the secondary database). The remaining 10 channels all exhibited strong I_p dependencies (coefficients up to 2.0). Hence, we note that *the central electron pressure is independent of the total plasma current*. Since the onset of I_p dependence occurs for those channels whose radii roughly correspond to minimum values of the sawtooth inversion radius ($r_{inv}(min) \simeq 1/q_a(max) = .30$ and $.24$ for the main and secondary databases respectively), we speculate that this I_p independence is coupled to sawtooth stability and sawtooth induced transport.

4.2 Temperature Profile Peaking Factor

Though we later analyse, as a function of radius, the bulk parameter dependencies of the local shape parameter $L_{T_e}^{-1}$, we present here results for the usual single-parameter measure of the temperature profile shape, namely the temperature profile peaking factor. We show that *the observed peaking factor is very close to that expected assuming a Spitzer resistive equilibrium*.

We first express the local cylindrical safety factor $q(r)$ as

$$q(r) = \frac{rB_{tor}}{RB_{pol}(r)} = \frac{2\pi r^2 B_{tor}}{\mu_0 R I(r)} = \frac{2B_{tor}}{\mu_0 R \langle J \rangle_r} \quad (1)$$

where $\langle J \rangle_r = \frac{1}{\pi r^2} \int_{r'=0}^r J(r') 2\pi r' dr'$ is the current density averaged up to radius r .

Assuming a classical resistive equilibrium, we immediately have that

$$\frac{\langle T^{3/2} \rangle_r}{\langle T^{3/2} \rangle_{r=1}} \simeq \frac{q_{r=1}}{q_r} \quad (2)$$

where the uncertainty arises from the fact that we neglect radial variations (assumed weak) in Z_{eff} or the Coulomb logarithm. Since all profiles are sawtoothing, we have $q(r < r_{q=1}) \simeq q_0$, a constant with a value close to unity. Hence we expect the 3/2 moments peaking factors, $\langle T^{3/2} \rangle_{r \simeq 0} / \langle T^{3/2} \rangle_{r=1}$ to scale as q_a . Since the YAG channel closest to the magnetic axis lies typically on the 14% flux radius, T_0 is essentially an extrapolated quantity. We present, therefore, scalings for the LHS of eq. (2) at both $r = 0$ and $r = .2$ where the latter radius satisfies the double requirement of being safely inside the inversion radius for all profiles as well as lying in the data region. For the main database, we obtained

$$\frac{T_0^{3/2}}{\langle T^{3/2} \rangle_{r=1}} = 1.02(\pm .06) \bar{n}_e^{.03 \pm .02} I_p^{.11 \pm .09} q_a^{1.13 \pm .06} \quad \text{RMSE} = .06 \quad R^2 = .874$$

$$\frac{\langle T^{3/2} \rangle_{r=.2}}{\langle T^{3/2} \rangle_{r=1}} = .99(\pm .04) \bar{n}_e^{.03 \pm .015} I_p^{.07 \pm .06} q_a^{1.07 \pm .04} \quad \text{RMSE} = .04 \quad R^2 = .931$$

while the secondary database yielded

$$\frac{T_0^{3/2}}{\langle T^{3/2} \rangle_{r=1}} = .96(\pm .17) \bar{n}_e^{.15 \pm .11} I_p^{-.12 \pm .26} q_a^{1.07 \pm .14} \quad \text{RMSE} = .10 \quad R^2 = .795$$

$$\frac{\langle T^{3/2} \rangle_{r=.2}}{\langle T^{3/2} \rangle_{r=1}} = 1.09(\pm .10) \bar{n}_e^{.13 \pm .07} I_p^{-.07 \pm .10} q_a^{.95 \pm .09} \quad \text{RMSE} = .06 \quad R^2 = .883$$

Since, for all four regressions, the \bar{n}_e and I_p coefficients are at best marginally significant at the 95% level, the results indeed strongly indicate that the peaking factor (eq. (2)) is determined solely by q_a . We now assume a sole q_a

dependence and re-do the regressions to get a tighter confidence interval for the constant factor and the exponent. For the high density database we get

$$\frac{T_0^{3/2}}{\langle T^{3/2} \rangle_{r=1}} = .94(\pm.04)q_a^{1.07\pm.04} \quad \text{RMSE} = .06 \quad \text{R}^2 = .866$$

$$\frac{\langle T^{3/2} \rangle_{r=.2}}{\langle T^{3/2} \rangle_{r=1}} = .93(\pm.03)q_a^{1.03\pm.03} \quad \text{RMSE} = .04 \quad \text{R}^2 = .925$$

while the secondary database yielded

$$\frac{T_0^{3/2}}{\langle T^{3/2} \rangle_{r=1}} = .85(\pm.11)q_a^{1.13\pm.10} \quad \text{RMSE} = .10 \quad \text{R}^2 = .780$$

$$\frac{\langle T^{3/2} \rangle_{r=.2}}{\langle T^{3/2} \rangle_{r=1}} = .97(\pm.07)q_a^{.99\pm.07} \quad \text{RMSE} = .07 \quad \text{R}^2 = .870$$

In all four cases, the q_a exponent is unity to within two standard deviations. Similarly, the constant factors are within two standard deviations of unity (with the marginal exception of the second regression: $.87 \leq \text{const} \leq .99$). These results are consistent with, but more specific than the inequality

$$q_a^{2/3} \leq \frac{T(0)}{\langle T \rangle} \leq q_a \quad (3)$$

derived by Waltz et al [15] using classical resistivity plus sawtoothing. Since we use $\langle T^{3/2} \rangle$ rather than $\langle T \rangle^{3/2}$, the upper and lower bounds of the inequality coincide in our case. To enable comparison with previous work, we regressed the more traditional peaking factor $T(0)/\langle T \rangle$ to obtain, for the combined database, the scaling: $T(0)/\langle T \rangle = 1.00(\pm.028)q_a^{.73\pm.030}$ whereas our normalisation gave (also for the combined database) $T(0)/\langle T^{3/2} \rangle^{2/3} = .99(\pm.028)q_a^{.67\pm.029}$. *We believe these results constitute strong evidence that the resistive equilibrium ansatz is sufficient to explain quantitatively the scaling of the peaking factor for ASDEX Ohmic temperature profiles.*

5. PROFILE SHAPE ANALYSIS

The next two sections are devoted to a detailed description of profile parameterisation techniques and the ensuing methods of data analysis, tailored to our case. For a more theoretical background, the reader is referred to KRML. The experimental results are presented in section 7.

We assume that the logarithm of the temperature satisfies $\ln T(r, q_a, I_p, \bar{n}_e) = \mu(r, \vec{x}) + \epsilon$ where ϵ is a random error. The deterministic part, $\mu(r, \vec{x})$, is represented as a spline with reasonably high resolution in the radial direction,

and a simple (polynomial-type) dependence on the plasma-parameters. *The coefficients of the representation are determined by fitting all profiles simultaneously in a weighted least squares regression.*

The temperature and density measurements are obtained using the AS-DEX sixteen channel YAG Thomson scattering diagnostic [5] with a sampling rate of 60 Hz. This system consists of sixteen spatial channels located in the vertical plane at $R = 1.63$ m. They are spaced at approximately 4 cm intervals from $Z = .200$ m to $Z = -.394$ m. We did not use the 16th channel which lies very close to or on the separatrix, as the measurement failed for the majority of profiles in this database. The radius (averaged over all profiles) of the flux surface passing through each channel is presented in column 2 of Tables III and V for the main and secondary databases respectively.

5.1. Radial Representations

In this subsection, we discuss continuous radial representations of plasma profiles. We consider data consisting of n separate compressed profiles of a spatially varying plasma variable such as temperature or density, at p distinct radial points. Each compressed profile is the average of $m = 12$ consecutive measurements taken at 17 msec intervals. We do, however, make use of the uncompressed profiles for the purpose of estimating the channel-by-channel raw measurement fluctuations within each discharge. Thus our temperature data can be described by $T_{i,j}(r'_l)$, where $i = 1, \dots, m$ labels the uncompressed timepoint, $j = 1, \dots, n$ is the compressed profile index, and $l = 1, \dots, p$ denotes the radial channel number. We make a preliminary transformation of the physical measurement locations r'_l to the corresponding flux surface radii r_l .

Continuous representations have the following characteristics: a) A large number of dependent variables, represented by point data, is replaced by a small number of coefficients which nevertheless will be sufficient to represent all significant features of the profiles. b) Profiles measured at two different sets of radial locations may be compared. This is relevant, e.g., where we wish to compare YAG temperature measurements with electron cyclotron emission (ECE) data measured at different spatial locations. c) Smoothness is imposed in the belief that the profiles are in diffusive equilibrium.

Instead of fitting the profile itself, we choose to fit its natural logarithm Y . Minimising the residual of the logarithm of the plasma profile corresponds to minimising the relative rather than the absolute error. Preliminary comparisons with low order spline or polynomial fits to the actual profiles revealed that the logarithmic fit tended to have not only smaller residual errors on the logarithmic scale but also on the usual physical scale. This indicates that the ‘exponentiated form’ of the logarithmic fit is a better approximation to the actual plasma profiles than a comparable low order fit to the linear profile. We note that the difference between logarithmic and linear fits decreases as more regression parameters (either spline knots or higher order polynomial terms) are added. Logarithmic fits have several other advantages. Firstly, the predicted profile can never be negative. Secondly, well-known power-law type scalings reduce to linear models. Finally, if the noise level is proportional to the absolute value of the measurement (an admittedly idealised situation), then, on the logarithmic scale, unweighted least squares may be used.

Spline representations, which we employ here for profile parameterisation, give flexibility in choosing between local resolution and compact global representation. The profile parameterisations presented in the present work are based on twice continuously differentiable splines with a selectable number of knots, ν . The profile is forced to be parabolic inside the first knot, i.e. the region enclosing the magnetic axis. The radius is decomposed into $\nu + 1$ regions with knots at r_1, r_2, \dots, r_ν . Such a profile may be parameterised

explicitly by:

$$\mu(r) = \begin{cases} \mu(r_1) + \mu''(0)(r^2 - r_1^2)/2 & \text{for } 0 \leq r \leq r_1 \text{ (Inner Region)} \\ \mu(r_1) + \mu''(0)(r^2 - r_1^2)/2 + c_1(r - r_1)^3 & \text{for } r_1 < r \leq r_2 \text{ (Region 1)} \\ \mu(r_1) + \mu''(0)(r^2 - r_1^2)/2 + c_1(r - r_1)^3 \\ \quad + c_2(r - r_2)^3 & \text{for } r_2 < r \leq r_3 \text{ (Region 2)} \\ \dots\dots\dots & \dots\dots\dots \\ \mu(r_1) + \mu''(0)(r^2 - r_1^2)/2 + c_1(r - r_1)^3 \\ \quad + c_2(r - r_2)^3 + \dots + c_\nu(r - r_\nu)^3 & \text{for } r_\nu < r \leq 1 \text{ (Outer Region)} \end{cases} \quad (4)$$

In more compact fashion, we express the spline $\mu(r)$ as

$$\mu(r) = \sum_{k=-1}^{\nu} \alpha_k H(r_k) \varphi_k(r) \quad (5)$$

where ν is the number of knots used, α_k represent the spline parameters:

$\mu(r_1), \mu''(0), c_1, c_2, \dots, c_\nu$; $\varphi_k(r)$ are the polynomials: $\varphi_{-1}(r) = 1$, $\varphi_0(r) = (r^2 - r_1^2)/2$, $\varphi_1(r) = (r - r_1)^3$, \dots , $\varphi_\nu(r) = (r - r_\nu)^3$, and

$$H(r_k) = \begin{cases} 0 & \text{for } r < r_k \\ 1 & \text{for } r \geq r_k \end{cases} \quad (6)$$

is the Heaviside unit stepfunction ($r_k = 0, 0, r_1, r_2, \dots, r_\nu$).

As well as the parabolic restriction near the axis, a ‘natural’ spline boundary condition, $\mu''(1) = 0$, was imposed in practice. The spline fits were carried out using the SAS REG procedure [17] which contains convenient possibilities for restricted regression. A similar spline model for transport analysis of individual profiles has been used in [19].

5.2. Parametric Dependencies of Plasma Profiles

Since the plasma profile shapes depend on the bulk plasma variables such as q_a , the spline coefficients will be functions of these parameters. Since

our database is not expected to contain sharp transitions in behaviour in parameter space, a low order parametric representation is expected to be adequate. Therefore, *we approximate the smooth parametric dependencies of the profile shape by linear or possibly quadratic polynomials in the logarithms of the bulk variables.*

Let $\vec{x} = (x_1, x_2, x_3)$ be the vector consisting of the bulk plasma variables q_a, I_p, \bar{n}_e . We define the *linear basis functions* $g_0(\vec{x}) = 1$ (*intercept*), $g_j(\vec{x}) = \ln x_j/x_j^*$, $j = 1, 2, 3$; where x_j^* is a *representative value* of the variable x_j in the database of interest. For ease of comparison, we choose for both databases the same normalising values $q_a^* = 2.5$, $I_p^* = .4$ MA and $\bar{n}_e^* = .4 \times 10^{20} \text{m}^{-3}$, although these do not constitute a typical parameter set for the secondary database. By normalising the bulk variables to x_j^* , the value of the response variable at the intercept in the regression becomes the predicted value at $\vec{x} = \vec{x}^*$.

The full profile representation can be written as

$$Y(r, \vec{x}) = \sum_{k,j} \alpha_{k,j} g_j(\vec{x}) H(r_k) \varphi_k(r) + \epsilon \quad \equiv \mu(r, \vec{x}) + \epsilon \quad (7)$$

where ϵ is an error term, whose structure will be discussed in the next subsection. The basis functions are as defined before. Note that higher order terms can be included, if necessary, by extending the set of possible basis functions: $g_{j,l}(\vec{x}) = \ln x_j/x_j^* \ln x_l/x_l^*$, etc.

5.3. Error Structures:

In this subsection, we present and motivate the splitting-up of the total regression error into contributions that are attributable to different physical sources. An efficient analysis should take into account the particular features of such an error structure. In the next subsection, we discuss the methods of estimation we applied in our case.

We distinguish between several categories of random profile variations. We use the term ‘internal’ variations, to denote fluctuations on a time scale at least as fast as that of the diagnostic sampling rate. These include statistical noise from the measuring process and plasma fluctuations arising, in particular, from the $m = 1$ sawtooth instability. Discharge-to-discharge variations

are changes in the plasma profiles not observed within a single discharge. These discharge variations include effects such as impurity accumulation on the diagnostic windows and the condition of the plasma wall. These impurity and plasma wall effects tend to vary to an even larger extent from one experimental operating period to the next. In addition, discharges separated by a recalibration of the YAG system can exhibit systematic differences in the measured profiles.

As discussed in [12] appendix B, this hierarchy of temporal scales for plasma variation generates a compound error structure which can be treated statistically. We give a simplified discussion here. For convenience, we assume normally distributed errors, although this assumption can be relaxed in most of the discussion. Since the profiles in our database are already averaged over twelve consecutive time samples (see introduction), they no longer possess the same variance as the original uncompressed observations. For time averaged datapoints, $\bar{Y}(r, \vec{x}) = \frac{1}{m} \sum_{i=1}^m Y_i(r, \vec{x})$, the total unexplained variance can be decomposed into:

$$\sigma_{tot}^2 = \frac{\sigma_{int}^2}{m} + \sigma_{dis}^2 \quad (8)$$

where σ_{int}^2 is the variance of the internal or ‘within-discharge’ fluctuations of the uncompressed profiles, m is the number of timepoints in the compressed profile (in our case $m = 12$), and σ_{dis}^2 denotes the variance due to discharge-to-discharge variations.

To estimate the within-discharge variance $\hat{\sigma}_{int}^2$, we analysed the original uncompressed data and, for each channel, calculated the empirical variance for each 12-point set separately. We estimated $\hat{\sigma}_{tot}^2$ by regressing the set of n (compressed) datapoints for each individual measurement channel against the bulk variables and noting the unexplained variance. The difference, as given by the third term in eq. (8), is an estimate of the discharge-to-discharge variance.

In Tables III(b) – VI(b) columns 3 and 4, one can see the estimates of σ_{int} (scaled for compressed profiles) and σ_{tot} for each of the 15 channels. It is clear from the large channel to channel variation displayed in these tables,

that it would not be justified to make model assumptions that σ_{int} and/or σ_{tot} are the same for all channels.

5.4. Coefficient Estimation

We determine the spline coefficients, including parametric dependencies, by fitting all profiles simultaneously in a weighted least-squares regression where the weights, $W(r_l)$, depend on the channel location.

We wish to determine that vector of coefficients $\underline{\alpha}$ which minimises

$$\sum_{j,l} \left(Y_{j,obs}(r_l) - Y_{j,fit}(r_l, \underline{\alpha}) \right)^2 W(r_l) \quad (9)$$

where $W(r_l)$, $l = 1, \dots, 15$ are appropriately chosen weights for each of the 15 YAG channels. We investigated two approaches for determining $W(r_l)$. In the first method, we rely on the total unexplained variance for each channel (as discussed in the previous subsection) as a measure of the channel weighting: $W(r_l) = \hat{\sigma}_{tot}^{-2}(r_l)$. A second approach to the selection of the regression weights, is the iterative estimation of the residual variance of the spline fit at each channel. At the k^{th} iteration we have:

$$\hat{\sigma}_{(k+1)}^2(r_l) = \frac{1}{n} \sum_{j=1}^n \left(Y_{j,obs}(r_l) - Y_{j,fit(k)}(r_l, \hat{\underline{\alpha}}_k) - \delta \bar{Y}_k(r_l) \right)^2 \quad (10)$$

where $\delta \bar{Y}(r_l)$ is a possible systematic bias in fitting the l^{th} measurement channel which can be estimated by including an indicator dummy variable for each of the 15 channels in the regression. The inclusion of this term prevents undue downweighting of channels where the parameterised profile may consistently fail to match the observed data. For the first iteration, the variances $\hat{\sigma}_{(1)}^2(r_l)$, are initialised to unity (equal weights). The iteration is terminated after the third iteration. We then have $W(r_l) = \hat{\sigma}_{(last\ iter.)}^{-2}(r_l)$. If the regression model and the assumed error structure is correct, this is a likely to be a consistent and efficient estimate (see e.g. [20]). Nevertheless, we regard $\hat{\sigma}_{tot}^{-2}(r_l)$ as a more robust estimate than $\hat{\sigma}_{(last\ iter.)}^{-2}(r_l)$ since it depends only on the fit by the bulk variables whereas the latter estimate also depends on the spline model and has the additional problem of the strong

(anti)correlation of outer channel residuals. Accordingly, we preferred to use $W(r_l) = \hat{\sigma}_{tot}^{-2}(r_l)$. The dominant effect of this reweighting is to decrease the influence of the channels near the plasma boundary where the relative error is largest.

5.5. Criteria for Additional Free Parameters

In the context of profile parameterisation, some relevant statistical tests for the significance of including additional variables are discussed in KRML. In the case of independent errors, these criteria are given by the F test [6] and Mallows C_p statistic [24]. Mallows C_p statistic is the sum of the total bias in the regression and the total variance of the predicted values. As more free parameters are added, the bias decreases but the variance increases. To determine whether to add another parameter, one can look at the change in the C_p statistic or apply the F test.

It should be noted that in practice these statistical approaches may either under- or overestimate the significance of the additional variables since the correlations in the errors are neglected. In addition, these tests neglect systematic errors and assume that the ideal data, without measurement errors, is exactly describable by the regression equation under consideration. Thus many spurious dependencies may be included and real dependencies missed by unthoughtful or automated use of these methods.

6. PROFILE PARAMETERISATION TECHNIQUES

In this section, we discuss a number of practical aspects encountered during our investigation, which are expected to be useful in any profile analysis. Logarithmic representations are employed throughout, for the reasons outlined in subsection 5.1.

6.1. Polynomial Models

Initial efforts concentrated on fitting polynomial representations of the form:

$$T(r) = T_0 \exp(ar^2 + br^4 + cr^6)$$

This model was successful in reproducing the general properties of the AS-DEX profiles, but not detailed features. Sharp gradients and local flattenings

(due, perhaps, to magnetic islands) were poorly modelled. A disadvantage of the above model, exacerbated by the addition of higher order polynomial terms, is the insensitivity of the inner region to r^4 and higher powers as well as the high degree of stiffness of these polynomials. To enable us to fit each region of the profile in moderate powers of the radial coordinate, we turned to spline representations.

6.2. Once and Twice Continuously Differentiable Cubic Splines

Following [21] we first used a five parameter, two knot Hermitian spline, i.e. one with no continuity requirement on the second derivative. This turned out to be clearly better in parameterising steep gradients and abrupt spatial transitions in profile shape than the polynomial model. By experimentation, we found that a total of four knots, requiring seven regression parameters, gave a practical balance between fitting accuracy and significance of the spline coefficients.

A serious disadvantage to the Hermitian spline emerged, however. By allowing discontinuous second derivatives at the knots, continuous transitions in plasma behaviour were modelled as sharp jumps across knot boundaries. This effect was especially prominent in the slope of the inverse fall-off length as a function of q_a . After some investigation, we opted instead for the twice continuously differentiable spline model, eq. (4).

6.3. Spline Knot Locations and Boundary Conditions

The knot positions are chosen such that the measuring channels are distributed roughly equally in the various regions between and outside of the knot positions. Too many knots result in spuriously oscillatory fits. The knot locations were varied manually to achieve a near ‘optimal’ fit as determined by the balance between goodness of fit and significance of the fit coefficients. We decided on a set of five knots at the following locations: $r_{knot} = .2, .3, .4, .5, .65$.

The innermost channel is typically located at $r = .14$ and the outermost channel at $r = .89$ (Table III column 2). When third degree polynomials were used in the innermost and outermost regions, the extrapolated curves (to $r = 0$ and $r = 1$ respectively) had unphysical oscillations. These oscillations were eliminated by reducing the number of free parameters for these

regions. Near the origin, the profile was forced to be parabolic (this is already enforced in eq. (4)). The so-called natural boundary condition, $\mu''(1) = 0$, was applied at $r = 1$. We investigated the regression fits with the natural boundary conditions applied to (a) all spline coefficients (b) bulk parameter-dependent spline coefficients only. Case (a) resulted in considerably higher fitting errors than case (b) for, in particular, the outer channels of the main database density profile fit. However, we concluded that the improvement in case (b) was at the expense of overfitting of the outer channels and we present here only the results of the fully applied boundary conditions. In a preliminary version of this work [12], the results of case (b) are presented. Thus our 5-knot set yields a model of seven spline coefficients with one boundary constraint per bulk parameter basis function used in the fit. The profile parameterisations presented later were carried out using the linear basis functions $g_j(\vec{x})$, $j = 0, 1, 2, 3$, only. Some quadratic and cross terms were very significant in preliminary regressions involving both databases simultaneously. For reasons given in the introduction, however, the results we present come from separate profile shape analyses for each database. For these regressions, second order terms were rarely significant and the goodness of fit was scarcely affected by the restriction to linear terms. Using the three bulk parameters q_a , I_p and \bar{n}_e , we have a regression model with a total of (intercept + 3 bulk parameters) \times (7 radial coefficients - 1 boundary condition) = 24 degrees of freedom to fit (e.g. for the main database) $15 \times 105 = 1575$ individual temperature (or density) data. With the foregoing boundary conditions, this spline representation tended to be stable in extrapolating profile behaviour into regions where there were no measurement channels.

6.4. Normalisation

The goal of our profile analysis is to determine the dependence of the profile shapes, i.e. the functions $L_{T_e}^{-1}(r) = \frac{1}{T_e} \frac{d}{dr} T_e(r)$ and $L_{n_e}^{-1}(r) = \frac{1}{n_e} \frac{d}{dr} n_e(r)$, $0 < r < 1$, on the plasma parameters. This brings up the problem of fitting the profile size. We found that when we made a simultaneous fit of the size and the shape of the profile, the residual sum of squares was dominated by the uncertainty in fit of the profile size. Therefore, a model was fitted which provided a free parameter to fit each individual profile size. This normal-

isation procedure, justified because the profile size scales out of the profile shape definition above, causes very significant reductions in the residual sum of squares of the shape regressions.

Originally, we normalised each profile by its line-average, calculated from the spline fit. This greatly reduced, but did not minimise, the residual error in the profile parameterisation since the line-average is itself a function of the profile shape. Instead, we estimated the profile size parameters, using the SAS procedure GLM [17], by treating the profile index as an indicator variable. This yielded as normalising factor the radially independent term in our spline representation, i.e. $\mu(r_1)$, the profile value at the first knot which is sited at $r = .2$. Normalisation has the effect of reducing by one the number of degrees of freedom for each individual spline. Hence, the total number of degrees of freedom for the 5-knot spline with coefficients dependent on 3 bulk parameters (as described in the previous subsection) is reduced from 24 to 20.

6.5. Operating Period Indicator Variable

In the course of determining $\hat{\sigma}_{tot}^2(r_l)$ for each YAG channel, plots of residuals versus shot number revealed that the secondary database residuals, whose discharges spanned a period of over six months in contrast to the one week span of the main database, fell into four distinct groupings which we ascribe to four distinct experimental operating periods (see introduction). This 4-cluster formation was observed for all 15 channels, although the pattern formed by the clusters differed for each channel. To remove this operating period contribution to the overall unexplained channel variances for this database, and hence to enable a comparison to be made between the two databases, separate indicator variables for each operating period were added in the individual channel regressions used to determine $\hat{\sigma}_{tot}^2$. These indicator variables were not, however, included in the profile shape regressions. To do so would have required an additional 60 independent variables (4 for each channel) which, in our judgement, would have led to overfitting of the profiles.

6.6. Examination of Outliers

Apart from the operating period effects mentioned above, plots of raw

versus fitted data for the same channel-by-channel regressions revealed that a small number of individual channel measurements from both databases produced strongly outlying residuals (the worst case was one of 8.5 standard deviations). To arrive at a quantitative criterion for identifying suspect data, we analysed the Studentised residuals. A Studentised residual is the difference between the observed and fitted value, normalised to the RMSE. For normally distributed errors, they have approximately a standard normal distribution. If we consider a single Studentised residual, the probability that it lies outside $\pm c$ is ϵ , where $\epsilon \simeq 1 - (2\pi)^{-\frac{1}{2}} \int_{-c}^{+c} e^{-x^2/2} dx$. Considering now n uncorrelated residuals together, we have that the probability of all n residuals lying *inside* $\pm c$ is $(1 - \epsilon)^n$. Hence the probability of at least one among n Studentised residuals lying outside $\pm c$ is given by $1 - (1 - \epsilon)^n = \beta$, say. Provided the correct model is used to fit the data, we suspect any outlier whose Studentised residual exceeds $\pm c_\beta$ for a suitably small β (using $\epsilon = 1 - (1 - \beta)^{1/n} \simeq \beta/n$ for $\beta \ll 1$, we invert the probability integral to determine c_β). We chose $\beta = 1\%$ which, for $n = 105$ and $n = 38$, yields $c = 3.90$ and $c = 3.64$ for the main and secondary databases respectively. Using this criterion, we identified 6 suspect outliers from the main database and 18 from the secondary, amounting to 0.2% and 1.5% of the data respectively.

Profiles containing any suspect observations were now examined individually. In most cases it was visually obvious that the affected channel was inconsistent with the rest of the profile, and such observations were marked as bad data. One discharge accounted for the majority of the suspect data in the secondary database. On inspection, it was clear that the quality of the profile data for this discharge was so poor, that it was excluded entirely from the subsequent analysis, thereby reducing the number of discharges from 38 to 37 for this database. On the other hand, several suspect observations from a single profile in the main database were not visually inconsistent with the rest of that profile's data. On investigating further, it turned out that this discharge had the highest B_t value (2.73 T) in the database. This highlights the need to examine all suspect outliers individually, since the influential position of this data suggests an inadequacy in the model used to fit the data rather than in the data itself, and its rejection would be quite unjustified.

The small number of observations finally deemed to be faulty (a total of 4 points affecting 3 profiles in the main database; 12 points affecting 9 profiles in the secondary database) were deleted from the regression.

6.7. Measurement Asymmetries

Ten of the fifteen YAG channels in ASDEX are located in nearly symmetric positions with respect to the horizontal midplane. By examining the residual errors for each channel separately, an up-down asymmetry was found in the density profile (up-down difference $\simeq 7\%$) The asymmetry was nearly uniform on all five pairs of measurement channels and was independent of plasma parameters. No significant asymmetry was found in the temperature profiles.

A likely explanation for this asymmetry was found after a routine inspection this year (1990). A slight misalignment of the laser beam direction against the entrance slits of the detectors may have decreased the sensitivity of the radial channels below the equatorial plane. Another possible cause is a spatially non-uniform distribution of impurities on the diagnostic window. Assuming that for the range of scattered laser light detected by the system ($0.8\mu m \leq \lambda_{scatt} \leq 1.06\mu m$), the impurity accumulation causes a spectrally uniform reduction in transmission, then the temperature, which is calculated from the ratio of the scattering signals of two spectral channels at the same spatial location, is insensitive to such asymmetries and only the density is affected.

To estimate and correct for this density profile asymmetry, we expanded the set of bulk parameter dependent, radial basis functions to include a single asymmetry indicator variable which takes the value of +1 for the channels above the midplane and -1 below the midplane. The final model, the results of which are presented in the next section, accordingly increases its degrees of freedom by one to give a total of 21 for the density profile regressions (the temperature model remains at 20 degrees of freedom).

7. EXPERIMENTAL RESULTS

7.1. Temperature Profile

In this subsection, we present a detailed graphical representation of our

results. The dominant shape dependency is a peaking of the profile inside $r = .6$ with increasing q_a . The profile shape shows very little dependence on any bulk parameter outside $r = .6$. Thus our result is similar to Fredrickson's [18] (profile shape invariant for $r \geq .4$) and Murmann's [22] (profile shape invariant for region outside influence of $q = 1$ surface), though our more elaborate model enables us to examine more sensitively the extent of the q_a dependent region.

In Figs. 5 and 6 we display, as a function of radius, the reference profiles and the parametric dependencies of the negative inverse fall-off length (IFOL), normalised to the inverse minor radius. Dashed curves indicate local 95% confidence bands. The corresponding global 95% confidence bands are, in this case, approximately 1.5 times wider. See KRML for a discussion on local and global confidence bands. By the term reference profile we mean the evaluation of the parameterised spline fit at the representative set of parameter values $\vec{x} = \vec{x}^*$ as discussed in section 5.2. Since the vector of basis functions $\vec{g}(\vec{x}) = (1, \ln x_1/x_1^*, \ln x_2/x_2^*, \ln x_3/x_3^*)$ reduces in this case to $\vec{g}(\vec{x}^*) = (1, 0, 0, 0)$, the reference profile is just that described by the set of intercept, i.e. bulk parameter-independent, spline coefficients.

The parametric radial dependencies of the IFOL are obtained by differentiating the parameterised spline representation for the normalised profiles both radially and with respect to the basis function of the desired parameter. Fig. 5(b), for example, shows the radial behaviour of the q_a dependence which, using eq. (7) (with $g_1(\vec{x}) = \ln q_a - \ln q_a^*$), is given by

$$\frac{\partial(-L_{T_e}^{-1})}{\partial \ln q_a} = -\frac{\partial^2 \mu(r, \vec{x})}{\partial g_1 \partial r} = -\frac{\partial}{\partial r} \sum_k \alpha_{k,1} H(r_k) \varphi_k(r) \quad (11)$$

We see that at $r \simeq .35$, where the profile shape is most sensitive to q_a , a unit change in $\ln q_a$ causes a change of $\simeq 5$ in the negative IFOL corresponding to 12.5 m^{-1} for an ASDEX minor radius of .4 m. Parametric dependencies of 'experimental' point values are also displayed. These are calculated by differencing the measurement values of pairs of neighbouring channels: $L_i^{-1} = \frac{T_{i+1} - T_i}{.5(T_{i+1} + T_i)(r_{i+1} - r_i)}$ and regressing these approximate IFOL's on q_a , I_p and \bar{n}_e . Such a point value has the advantage that it is more local than the

continuous function represented by eq. (11), but the disadvantage that the signal to noise ratio will be lower. The mean value will also be particularly affected by systematic errors in one or both of the adjacent channels.

The negative IFOL profiles for minimum, reference, and maximum q_a , displayed in Fig. 5(a), show that the temperature profile shape for the main database is remarkably invariant outside $r = .6$. This behaviour is broadly similar for the profiles of the secondary database. The larger error bands of the latter, reflecting the substantially higher regression error for this database, are due in large measure to the already discussed problem of multiple operating periods for this database. The parametric dependencies of the IFOL profiles are detailed in the remaining sub-figures.

The q_a dependence of the inverse fall-off length of both databases increases rapidly and *reaches a maximum near* $r = .35$. The strength of this q_a dependence then decreases sharply, and outside $r = .6$ the profile shape is independent of q_a . Between $.15 \leq r \leq .25$ the point estimates of the ‘experimental’ IFOL suggest a radially uniform q_a dependence. However, the large error bars allow for a slope between roughly -10 and 10 on the scale of the plot. Inside the first knot, our radial spline model consists of a parabola with $T'_0 = 0$. This requires the IFOL as well as each individual parametric dependency to describe a straight line through the origin in this region.

The I_p and \bar{n}_e dependencies are much weaker. Although, over some portions of the radius, rejection at the 5% level is marginally avoided, temperature profile invariance with respect to I_p and \bar{n}_e is generally seen to hold, within the experimental error limits, for all radii. Figs. 7 and 8 show reference profiles and parametric radial dependencies for the normalised profiles $\ln \hat{T}_e(r)$ (where $\hat{T}_e(r) = T_e(r)/T_e(r = .2)$). These are equivalent to the integrals of Figs. 5 and 6, with the integration constant chosen to give $T_e(r = .2) = 1$. The invariance of the profile shape outside $r = .6$ is reflected here by the fact that all profiles are parallel in this region (see Figs. 7(a), 8(a)) and all parametric dependencies (almost) horizontal (see Figs. 7(b)-7(d), 8(b)-8(d)).

We now consider the hypothesis that $T_e(r)$ has a Gaussian shape. Since, to a high approximation, the profile shape has been shown to be solely a

function of q_a , the most general family of admissible Gaussian profiles is:

$$T_e(r) = T_{e,0}(\bar{n}_e, I_p, q_a) \exp(-f(q_a)r^2) \quad (12)$$

where $f(q_a)$ is a positive function. The negative IFOL would then satisfy

$$-L_{T_e}^{-1} = -\frac{d}{dr} \ln T_e(r) = 2rf(q_a) \quad (13)$$

which describes a family of straight lines through the origin. *It is clear from Fig. 5(a) (and Fig. 6(a)) that this hypothesis is false for our data.* It is also visually obvious that even the q_a -independent part of the profile ($r > .6$) does not lie on a Gaussian. To quantify this, we made a regression of channels 12 – 15 (i.e. those roughly satisfying $r \geq .6$) normalised to their line-averaged value versus a Gaussian function, which gave $T_e(r \geq .6) = 3.76 T_e^{line\ av.}_{(r \geq .6)} \exp(-2.53r^2)$ with a RMS relative error of 5.4%. Adding a cubic term already strongly reduces the error: $T_e(r \geq .6) = 1.88 T_e^{line\ av.}_{(r \geq .6)} \exp(1.48r^2 - 3.62r^3)$ with a RMS relative error of 3.8% (F value for cubic term $\simeq 400$). Thus, even for the outlying portion of the profile, we can categorically rule out a Gaussian shape.

Figs. 9 and 10 show a sample experimental T_e profile from each database, representing extremes of the q_a range covered by our data. In each case, the predicted profile with 95% global confidence bands is also shown. Since we are concerned here with both profile size and shape recovery, these predictions come from a parameterised spline regression of *unnormalised* experimental profiles. Hence the confidence bands are wider (by $\simeq 50\%$) than those of the corresponding normalised profile predictions.

7.2. Temperature profile variance

We now examine how well the fitted profiles describe the data both in terms of root mean squared error and the fraction of data variance explained by the model. We also give a break-down of the profile fluctuations into within-discharge and discharge-to-discharge contributions.

Table III(a) presents some descriptive statistics for the temperature profiles in the main database on a channel-by-channel basis. Table V(a) displays the equivalent information for the secondary database. The channels are

numbered according to their vertical position with channel 1 at $Z = .200$ m, channel 6 at $Z = 0$ m, and channel 15 at $Z = -.353$ m. For each channel, the mean normalised flux radius is presented, followed by the mean temperature and the spread in keV. The spread (this term is chosen to avoid possible confusion with standard deviation in the sense of ‘regression error’) is just the ‘standard deviation from the mean’, i.e. $spread = \sqrt{\frac{1}{(N-1)} \sum_{i=1}^N (y_i - \bar{y})^2}$, where \bar{y} is the sample mean. Recall that before the regression, the profiles were normalised by the size parameter from the SAS GLM procedure, i.e. $T_e(r = .2)$, obtained from fitting each profile individually. Columns 5 and 6 present the mean and spread of these normalised profiles. Channels 5 and 8 have very small spreads since they lie closest to the normalisation radius.

As we are fitting on the natural logarithmic scale, it is of particular interest to tabulate the logarithmic, or relative, spread of the normalised profiles as a measure of the total variation of the data for each channel. This quantity, together with the channel-by-channel noise level estimates and RMSE’s resulting from our spline parameterisation of the temperature profiles is presented for the main database in Table III(b) and for the secondary database in Table V(b). In column 3, we display $\hat{\sigma}_{int}/\sqrt{12} \equiv \hat{\sigma}_{int, comp.}$; the estimated standard deviation of the within-discharge noise scaled for time-compressed profiles. Column 4 tabulates $\hat{\sigma}_{tot}$, the total noise level (of the compressed profiles), estimated by regressing $\ln T_e$ for each channel on the bulk parameters. The differences of the squares of the entries in column 4 and column 3 are an estimate of the discharge-to-discharge variance.

The ratio of the two noise estimates lies in the range $.2 \leq \hat{\sigma}_{int, comp.}^2/\hat{\sigma}_{tot}^2 \leq .5$ indicating that the discharge-to-discharge variance is the dominant contribution to $\hat{\sigma}_{tot}^2$. Using eq. (8) and the RMS values (over the 15 channels) for $\hat{\sigma}_{int, comp.}$ and $\hat{\sigma}_{tot}$, we find that for the main database, $\hat{\sigma}_{dis}(rms) \simeq 3.6\%$. For the secondary database, $.1 \leq \hat{\sigma}_{int, comp.}^2/\hat{\sigma}_{tot}^2 \leq .6$ and we have $\hat{\sigma}_{dis}(rms) \simeq 4.5\%$.

To indicate how much bias is introduced by our spline model, we also carried out channel-by-channel regressions of the normalised profiles. This is equivalent to using an interpolating radial spline. The RMSE’s for these

regressions appear in Table III(b) column 5. The RMSE calculated for each channel from the parameterised spline regressions appear in column 6. The generally close agreement between columns 6 and 5 ($\hat{\sigma}_{spline}(rms) = .030$; $\hat{\sigma}_{channel}(rms) = .028$) confirms the adequacy of the 5-knot spline model. The largest discrepancies occur for channels 2 and 10 which form one of the five up-down symmetric channel pairs. On inspecting the bias (systematic deviation from the regression line) for each channel, it was found that channels 2 and 10 had by far the largest bias (-3.3% and $+2.9\%$ respectively; the next largest channel bias was 1.2%), indicating that at least one of these channels suffered from a systematic error of up to 6% . In contrast to the main database, the spline regression errors in the secondary database (see Table V(b) column 6) are, in general, much larger than the channel-by-channel errors in column 5 ($\hat{\sigma}_{spline}(rms) = .069$; $\hat{\sigma}_{channel}(rms) = .039$). This is explained by the fact that, unlike the channel-by-channel regressions, we did not use operating period indicator variables in the spline parameterisation of the secondary database profiles (subsection 6.5). For both databases, the regression errors generally increase for outlying channels, reflecting a progressively deteriorating signal-to-noise ratio. This is due to the decrease in scattered laser light signal intensity with decreasing electron density. Note that channel 12 is an exception, with errors similar to channel 15. This is consistent with the fact that, whereas all other channels had three distinct spectral filters (normally offering the choice of the less noisy of two independent determinations of the temperature), channel 12, at the time the discharges for our databases were made, had only two.

7.3. Density

Since many of the results presented in the last section apply to the density profiles as well, we only mention the differences. Tables IV and VI contain the density statistics for the main and secondary databases respectively.

Figs. 11 and 12 portray graphically our parameterisation of the density profile local shape parameter $-L_{n_e}^{-1} = -d \ln n_e / dr$ for each database. Figs. 13 and 14 show the integrals of Figs. 11 and 12, i.e. the normalised density profile parameterisations. Figs. 15 and 16 show sample experimental n_e profiles (with prediction profiles and confidence bands) for the same discharges

which provided the sample T_e profiles shown in Figs. 9 and 10. Note the ‘jump’ in the predicted profiles at $r = 0$, which arises from the presence in the regression of the density up-down asymmetry variable (subsection 6.7).

The dominant feature of the density IFOL profiles (Figs. 11 and 12) is a q_a dependence closely mirroring that of the temperature IFOL, though at a reduced magnitude ($-\frac{\partial(L_T^{-1})}{\partial \ln q_a}(max) \simeq 5$; $-\frac{\partial(L_n^{-1})}{\partial \ln q_a}(max) \simeq 2$). The radial region over which it is significant ($.25 < r < .55$ for the main database) is smaller than the equivalent region for the temperature. Thus the variation of density profile shape with q_a , while not as dramatic as that of the temperature, is nonetheless considerable, as is evident in the contrast between Figs. 15 and 16. The magnitude of the density IFOL remains smaller than that of the temperature over the entire profile. At $r = .9$ it takes values between 2 and 3 (fall-off lengths between 20 cm and 13.3 cm for a minor radius of .4 m) whereas the temperature fall-off length at $r = .9$ is nearly fixed at $L^{-1} \simeq 5.5$ (see Fig. 5(a)), i.e. a fall-off length of about 7 cm for $a = .4$ m. As was the case with the temperature profile, the I_p and \bar{n}_e shape dependencies are weaker than that of q_a . Near the edge, however, there is a statistically significant *broadening of the density profile shape with increasing current*. (We note with caution, however, that the ‘experimental’ IFOL datapoints suggest that this current dependence is due solely to the outermost channel.) In addition, some flattening of the density profile with increasing \bar{n}_e occurs in the region $.5 < r < .7$.

For both databases, as can be seen from the RMS values for $\hat{\sigma}_{int, comp.}$ and $\hat{\sigma}_{tot}$, the discharge-to-discharge variance ($\hat{\sigma}_{dis}(rms) \simeq 2.2\%$ for the main database, and $\simeq 3.2\%$ for the secondary) forms the largest contribution to the total variance, as was the case for the temperature profiles. The overall spline regression RMS relative error for each database (.032 and .065) is very similar to the corresponding temperature value.

A number of density profiles in both databases are slightly hollow in the region $.3 < r < .4$. Since the set of reference profile parameters ($q_a^* = 2.5$, $I_p^* = .4$ MA and $\bar{n}_e^* = .4 \times 10^{20} \text{m}^{-3}$) was not very typical for the secondary database, this feature looks somewhat exaggerated for that database (see Figs. 12(a) and 14(a)).

7.4. Electron Pressure

The analysis of the (logarithmic) electron pressure profiles, defined as $\ln P_e = .4055 + \ln T_e + \ln n_e$, offers additional insight, as can be seen from the parametric dependencies shown in Figs. 17-20. For the main database, the most striking feature is that the I_p dependence is significant over most of the radius. In the outer region of the plasma, there is a clear broadening of the pressure profile with the current, while peaking occurs in the region $.2 < r < .4$. The q_a dependence of the inner half of the profile is very strong (temperature and density profile dependencies reinforce each other) whereas the \bar{n}_e dependence is little changed from that of the density profile.

8. DISCUSSION AND SUMMARY

Bulk scalings

In the first part of this work, we presented and compared the scalings of various global plasma parameters for two complementary ohmic datasets. For the main, high density database, the volume-averaged temperature and three independent measurements of the total plasma energy depend on the plasma current I_p and line-averaged density \bar{n}_e , but, at constant I_p and \bar{n}_e , are practically unaffected by the toroidal magnetic field. For the secondary database, Wp_{dia} and Wp_{mhd} show strong q_a scaling differences, while the Wp_{kin} and $\langle T_e \rangle$ scalings are almost the same as in the main database. The nearly linear current dependence for both the temperature and the total energy is reminiscent of L mode scaling.

The Spitzer Z_{eff} depends on all three control variables. Regression of $Z_{eff} - 1$ indicates, for both databases, that the impurity density is almost independent of \bar{n}_e , but strongly dependent on both I_p and B_t . The electron temperature profile peaking factor $T_0^{3/2}/\langle T^{3/2} \rangle$ scales as $.94(\pm .04)q_a^{1.07\pm .04}$, in close agreement with the prediction of classical resistive equilibrium.

The strong dependencies on the plasma current I_p of both the total plasma energy Wp and the Ohmic power approximately cancel to give a relatively weak current scaling for τ_E . Replacing (B_t, I_p) by (q_a, BI) gives a τ_E scaling

with a weak dependence on \bar{n}_e , a moderate dependence on q_a and with no statistically significant $B_p I_t$ dependence. In the range $.3 < \bar{n}_e/10^{20}\text{m}^{-3} < .8$, we detected little dependence of the global confinement time on the density. In particular, the *decrease* in the rollover regime with density as reported by [13], was *not found*. It should be remarked that the SOC data for $\bar{n}_e > 0.5 \times 10^{20}\text{m}^{-3}$ in [13], first reported in [14], is based on a single scan with $I_p = 0.42\text{MA}$, $B_t = 2.2\text{T}$. Obviously some scans show confinement deterioration, while others show a flat or even weakly improving τ_E versus \bar{n}_e dependence. The same phenomenon can be observed in plots from the Doublet III analysis [16]. The reason for this variability in SOC density scaling is at present unclear, and it requires further investigation.

Profile analysis

A careful statistical analysis is necessary to determine the radially varying parametric dependencies of the profile shapes on the bulk plasma variables. By simultaneously fitting all profiles with spline coefficients which depend on the plasma variables, we have been able to examine profile dependencies on a detailed, quantitative level. Based on this spline model, a convenient graphical representation has been used to inspect visually the influence of the various plasma parameters on the profile shapes.

An earlier study of ASDEX temperature profile shapes [22] (for both Ohmic and neutral beam heated discharges) revealed that the shape depends strongly on q_a inside the sawtooth mixing radius, but is almost independent of plasma parameters outside ‘the influence of the $q = 1$ surface’. The results of our profile parameterisation are roughly consistent with, and constitute a refinement of this analysis, for Ohmic profiles.

Except for a dependency of the outer region of the density profile shape on plasma current (and to a lesser extent on \bar{n}_e), the I_p and \bar{n}_e dependencies of both the temperature and density profile shapes are rather weak in general. In most cases the current and density dependencies are not significant given the error bars of the datasets.

In the interior, q_a is the dominant bulk plasma parameter in determining the temperature shape. By $r = .5$, however, this dependence has weakened considerably and outside $r = .6$, as is clear from Fig. 5, the IFOL profile

has an invariant shape. We note that the extent of the q_a -sensitive region is reasonably consistent with the widest sawtooth inversion radius in each database ($r_{inv}(max) \simeq 1/q_a(min) = .54$ and $.42$ for the main and secondary databases respectively).

Comparing Figs. 11 and 5, we see that the variation in the density profile shape, while significant, is much weaker than that of the temperature. This follows from the result that, over the inner half of the radius, the sensitivity of the density IFOL to q_a is only $\simeq 40\%$ that of the temperature. The q_a dependence is only significant for $.25 \leq r \leq .5$. In contrast to the temperature shape, which is unique outside $r = .6$, the density profile broadens significantly near the edge with increasing current.

The electron pressure IFOL exhibits a very strong q_a dependence in the inner half of the profile, while increasing I_p causes a broadening of the outer half, a tendency which intensifies approaching the plasma boundary.

Our findings are well described in terms of profile invariance [1, 21] and in quantitative agreement with important criteria for profile consistency as described by [4] and developed by many authors. However, we have not addressed the relative merits of profile consistency versus local transport models [10, 11] containing sawtooth effects. This issue could be addressed by a statistical comparison of experimental profile dependencies with the dependencies predicted by local transport models.

ACKNOWLEDGEMENTS

The work of PJM was performed under a EURATOM supported reciprocal research agreement between IPP and University College, Cork. The work of KSR was supported by the U.S. Department of Energy, Grant No DE-FG02-86ER53223. We are indebted to the referees, who made several critical suggestions from which the manuscript has profited considerably.

APPENDIX A ON STATISTICAL SIGNIFICANCE OF REGRESSION VARIABLES

The significance of a regressor x_j in the least squares model can be inter-

preted in terms of $\hat{\alpha}_j/\hat{\sigma}(\hat{\alpha}_j)$, the ratio of the fitted coefficient to its standard error estimate. Under standard least squares assumptions, including (a) the correctness of the regression model and (b) normally distributed errors in the dependent variable, the ratio $\hat{\alpha}_j/\hat{\sigma}(\hat{\alpha}_j)$ has a Student's t distribution under the null-hypothesis that $\alpha_j = 0$. For any statistic T that has a t distribution with f degrees of freedom, the following relation between the critical value $t_{f,\epsilon}$ and the 'exceedence probability' or significance level ϵ holds:

$$P\left\{|T| > t_{f,\epsilon}\right\} = \epsilon \quad (A1)$$

The null-hypothesis $\alpha_j = 0$ is rejected, and the regressor is considered significant, if $|\hat{\alpha}_j/\hat{\sigma}(\hat{\alpha}_j)| > t_{f,\epsilon}$ for some small value of ϵ , say 5%. For many degrees of freedom ($f > 30$ usually suffices) as in the present case, Student's t can be well approximated by the normal distribution. Thus we have $t_{f, .05} \simeq 2.0$, and the significance criterion is $|\hat{\alpha}/\hat{\sigma}(\hat{\alpha})| > 2.0$. This result is no longer exact, though still approximate, for mild violations of the normality assumption. A seriously deficient model can, however, invalidate this interpretation of the coefficient standard errors.

It is often useful to have an estimate of the contribution to the overall R^2 from each independent variable. Without loss of generality, we consider the multiple linear regression problem

$$y = \alpha_1 x_1 + \alpha_2 x_2 + \dots + \alpha_p x_p + \epsilon \quad (A2)$$

with centered dependent and independent variables. If the independent variables are uncorrelated, i.e. if $\langle x_j, x_k \rangle \equiv \sum_{i=1}^N x_{i,j} x_{i,k} = \|x_j\|^2 \delta_{j,k}$, it is easily shown that the least squares solution reduces to

$$\hat{\alpha}_j = \frac{\langle x_j, y \rangle}{\|x_j\|^2}; \quad \hat{\sigma}^2(\hat{\alpha}_j) = \frac{\hat{\sigma}^2}{\|x_j\|^2} \quad (A3)$$

Here $\hat{\sigma}(\hat{\alpha}_j)$ is the estimate of the standard error for the coefficient estimate $\hat{\alpha}_j$ and $\hat{\sigma}^2 = \|y - \hat{y}\|^2/(N - p)$ is the mean square regression error. From the definition of the t statistic, we have that

$$t_j \equiv \frac{\hat{\alpha}_j}{\hat{\sigma}(\hat{\alpha}_j)} = \frac{\langle x_j, y \rangle}{\|x_j\| \hat{\sigma}} = \frac{\sqrt{N-p} \langle x_j, y \rangle}{\|y - \hat{y}\| \|x_j\|} \quad (\text{A4})$$

In geometrical terms, $\langle x_j, y \rangle / \|x_j\|$ is the projection of y onto x_j where y and x_j are vectors in \mathfrak{R}^N . Hence, adding x_j to the regression model makes a fractional contribution to the total variance of

$$\Delta(\text{R}^2)_j = \frac{\langle x_j, y \rangle^2}{\|x_j\|^2 \|y\|^2} \quad (\text{A5})$$

Noting that

$$1 - \text{R}^2 = \frac{\|y - \hat{y}\|^2}{\|y\|^2} \quad (\text{A6})$$

we can use eqs. (A4) and (A6) to eliminate all terms involving x_j or y in eq. (A5) and we finally obtain

$$\Delta(\text{R}^2)_j = \frac{t_j^2}{N-p} (1 - \text{R}^2) \quad (\text{A7})$$

where the LHS denotes the decrease in R^2 if the j^{th} regressor is removed from the model. Note this relationship strictly holds only for uncorrelated regressors. If we now sum up all contributions, we obtain, using Pythagoras' theorem,

$\sum_{j=1}^p \langle x_j, y \rangle^2 / \|x_j\|^2 = \|\hat{y}\|^2$ which leads to the equality

$$\sum_{j=1}^p t_j^2 = (N-p) \frac{\|\hat{y}\|^2}{\|y - \hat{y}\|^2} = (N-p) \frac{\text{R}^2}{1 - \text{R}^2} \quad (\text{A8})$$

This formula is the analog of Weisberg's partition of C_p [23]. It provides a useful practical check on the applicability of eq. (A7) when the regressors are correlated, which is usually the case.

APPENDIX B

COMPOUND ERROR STRUCTURES: TEMPORAL HIERARCHY

To efficiently estimate the spline coefficients, $\underline{\alpha}$, we try to model the actual covariance matrix for the errors. The closer the assumed or estimated $\underline{\underline{\Sigma}}$ is to the actual covariance error structure, the more accurate the ensuing estimates for $\underline{\alpha}$ are.

The assumption of independent errors is not always justified. In general, tokamaks possess a compound error structure. The first level of errors are statistical fluctuations which vary from time point to time point within a given discharge. The next level consists of those errors which vary from discharge-to-discharge (we assume here that there is only one compressed datapoint per discharge) but remain constant within a given discharge. Finally, there are variations which only change between operating periods of a tokamak. We denote the covariance matrices of for the radial fluctuations of each of these three types of errors by $\underline{\underline{\Sigma}}^{int}$, $\underline{\underline{\Sigma}}^{disch}$, $\underline{\underline{\Sigma}}^{op}$ respectively.

We use a triple index, (p, i, t) to denote a given profile timepoint where p indexes the operating period, i the discharge number, and t the time. Within a single profile timepoint, the individual radial measurements are denoted by a fourth index, l . The cross-correlation of any two pairs of profile measurements, (p, i, t) and (p', i', t') is given by a 15×15 matrix, $\underline{\underline{\Sigma}}_{p,i,t,p',i',t'}$.

We assume that the errors do not depend on the plasma parameters and that the covariance structure does not vary between different blocks of data at each level. The most general error structure of this form is

$$\underline{\underline{\Sigma}}_{p,i,t,p',i',t'} = \underline{\underline{\Sigma}}^{int} \delta_{p,p'} \delta_{i,i'} \delta_{t,t'} + \underline{\underline{\Sigma}}^{disch} \delta_{p,p'} \delta_{i,i'} + \underline{\underline{\Sigma}}^{op} \delta_{p,p'} \quad (B1)$$

We restrict our attention to datasets consisting of a single operating phase. In this case eqn. (B1) reduces to $\underline{\underline{\Sigma}}^{int} \delta_{i,i'} \delta_{t,t'} + \underline{\underline{\Sigma}}^{disch} \delta_{i,i'}$. For simplicity, we assume that each discharge consists of n_t timepoints.

We estimate the within-discharge variance, $\underline{\underline{\Sigma}}^{int}$ empirically by calculating the time point average and the time point variance for each discharge separately:

$$\hat{\underline{\underline{\Sigma}}}_{k,l}^{int} = \frac{1}{n_d(n_t - 1)} \sum_{i=1}^{n_d} \sum_{t=1}^{n_t} (Y_{i,t}(r_k) - \bar{Y}_i(r_k))(Y_{i,t}(r_l) - \bar{Y}_i(r_l)) \quad (B2)$$

where

$$\bar{Y}_i(r_k) = \frac{1}{n_t} \sum_t Y_{i,t}(r_k) \quad (B3)$$

The disadvantage of analysing only the time averaged profiles is that information about the statistical fluctuations is lost. In an optimal statistical analysis, all time points would be retained and analysed simultaneously. This analysis may become unwieldy when the number of timepoints is large. However, if the timepoint variations are comparable to n_t times the discharge variation, a statistical analysis based on structured covariance matrices is desirable.

Within a single operating period, the total variation between datapoints is estimated by

$$\hat{\Sigma}_{k,l} = \frac{1}{n_d n_t - f} \sum_{i=1}^{n_d} \sum_{t=1}^{n_t} (Y_{i,t}(r_k) - Y_{fit}(r_k; \underline{\alpha})) (Y_{i,t}(r_l) - Y_{fit}(r_l; \underline{\alpha})) \quad (B4)$$

where f denotes the number of fitted parameters. The fitted values, $Y_{fit}(r_l; \underline{\alpha})$ depend on the values of the plasma parameters and therefore implicitly on the indices, i and t . $Y_{fit}(r_l; \underline{\alpha})$ may be estimated either by regressing each measurement channel separately or by fitting all channels simultaneously using the spline representation. The latter method will inflate the variance if the profiles cannot be well approximated by the spline representation.

The discharge variance is computed by subtracting the within-discharge variance as defined in eqn. (B2) from the total datapoint variance defined in eqn. (B4).

In describing nested error structures of this form, statisticians use the terms “within discharge variation” to refer to the time point to timepoint variation and “between discharge variation” for the discharge variation.

Several caveats must be placed on this procedure. First, using too many or too few terms in the regression analysis will artificially inflate the variance estimates. Second, the errors in the estimates of the variances tend to be rather larger unless a substantial number of profiles are available.

APPENDIX C

ANALYSIS FOR RADIALY CORRELATED ERRORS

When the random errors are correlated, the weighted least squares estimator is consistent but not efficient, i.e. as the number of datapoints approaches infinity, the estimates of the regression coefficients converge to their true value but the rate of convergence is not optimal.

To increase the precision of the estimate, one tries to model the actual covariance matrix for the errors. The closer the assumed or estimated $\underline{\underline{\Sigma}}$ is to the actual error structure, the more accurate the ensuing estimates for $\underline{\alpha}$ are. We continue to assume that the statistical fluctuations are temporally uncorrelated and neglect the parametric dependencies. However we now allow radial correlations in the fluctuations. Since the dataset consists of $15n$ datapoints, the entire covariance matrix is $15n \times 15n$. However we assume a block diagonal form for $\underline{\underline{\Sigma}}$ of the form:

$$\Sigma_{i,k,i',l}^{tot} = \Sigma_{k,l} \delta_{i,i'} \quad (C1)$$

where i, i' index the time-averaged profile and k, l index the channel number.

This covariance matrix of the residual radial errors may be estimated by:

$$\hat{\underline{\underline{\Sigma}}}_{k,l} = \frac{1}{n} \sum_i (Y_i(r_k) - \underline{Y}_{i,fit}(r_k, \underline{\alpha})) (Y_i(r_l) - \underline{Y}_{i,fit}(r_l, \underline{\alpha})) \quad (C2)$$

In the previous sections, we have assumed $\underline{\underline{\Sigma}}$ is diagonal. To examine whether our initial hypothesis of independent errors is reasonable, we perform a principal components analysis on $\hat{\underline{\underline{\Sigma}}}$.

If the condition number (the square root of the ratio of the largest to smallest eigenvalues) or the ratio of the arithmetic mean to the geometric mean of the eigenvalues is approximately one, then the previous analysis, based on radially uncorrelated fluctuations, is justified.

If the condition number is substantially larger than one, then the statistical estimating efficiency can usually be improved by prescribing a functional form, $\underline{\underline{\Sigma}}(\underline{\theta})$ to model the observed covariance. We can simultaneously estimate $\underline{\alpha}$ and $\underline{\theta}$ using maximum likelihood estimates [1].

APPENDIX D

Does Radius of q_a -dependent Region Contract as q_a Increases?

Since the sawtooth inversion radius decreases with increasing q_a , ($r_{inv} \simeq 1/q_a$ [?]), a natural hypothesis is that r_{tran} , the ‘transition radius’ where the temperature profile shape becomes independent of q_a , also scales with $1/q_a$. This question cannot be decided on the evidence of Figs. 2 and 3, beyond the assertion that for $r \geq .6$ the profile shape is q_a - independent for all values of q_a in the two databases. To make this analysis as radially localised as possible, while still attempting to satisfy the conflicting requirement that individual channel noise be smoothed out, we discarded the spline model used generally in this paper in favour of a moving average - type local quadratic fit (3 fit parameters) to successive groups of four neighbouring channels. To eliminate the possibility that the higher density of channels for $r \leq .5$ (due to the 5 channels lying above the midplane) might have a bearing on the results, we retained just the 10 channels on or below the midplane, resulting in seven groups per profile. By evaluating the local fits at intervals of $\frac{1}{40}$ radius (only that radial interval lying between the second and third channel in each group was used), a set of smoothed IFOLs was accumulated for each of the 142 experimental profiles in the combined database. These formed the working data for the following analysis.

To identify a possible q_a dependence of r_{trans} , we assume that r_{trans} is some simple function of q_a , e.g. $r_{trans} = \alpha_0 + \beta_0 q_a$, where the shape of the temperature profile is postulated to be q_a dependent inside r_{trans} only. The determination of the parameters α_0 and β_0 is a nonlinear problem which was handled by the following procedure:

- (i) Choose candidates α and β from a grid of possible values.
- (ii) For each (α, β) fit all profiles simultaneously with the scheme

$$L^{-1}(r, q_a) = \begin{cases} u(r, q_a) & \text{for } 0 \leq r < r_{trans} \\ v(r) & \text{for } r \geq r_{trans} \end{cases} \quad (20)$$

where $r_{trans} = \alpha + \beta q_a$ varies with each individual value of q_a , and $u(r, q_a)$ and $v(r)$ are quadratic functions of r : $u(r, q_a) = a_0 + a_1 q_a + (b_0 + b_1 q_a)r + (c_0 + c_1 q_a)r^2$ and $v(r) = d_0 + e_0 r + f_0 r^2$ with zeroth order continuity imposed

at $r = r_{trans}$.

(iii) Store α , β , and the mean square error (MSE) for each fit.

(iv) Locate $\hat{\alpha}_0$ and $\hat{\beta}_0$ giving the best fit (i.e. the global minimum MSE value).

(v) Make a contour plot of MSE as a function of (α, β) and hence determine the 95% confidence contour for $\hat{\alpha}$ and $\hat{\beta}$

(vi) If $\beta = 0$ lies inside the 95% confidence contour, then the null-hypothesis $\beta_0 = 0$ is compatible with the data.

The contour plot obtained using the above procedure is shown in Fig. 14. The global minimum MSE, $\hat{\sigma}_{min}^2 = .0906$, is given by $r_{trans} = .620 - .012q_a$.

To determine the 95% confidence contour for β where α is arbitrary, we use the result that the relative difference in the sum of squares has asymptotically a χ^2 distribution with, in our case, one degree of freedom (see [?] Chap. 5). For this analysis, because of the restrictions used in generating the input IFOL values, we have effectively 9 independent measurements per profile, giving a total (for 142 profiles) of $n = 1278$. From [?] Table C.1 we have $\chi_1^2(95\%) = 3.84$. This gives $\Delta(\text{RSS})_{95\% \text{contour}} = 3.84 \times \hat{\sigma}_{min}^2 = .348$. Hence the 95% contour has the values $\hat{\sigma}_{95\%}^2 = .0906 + .348/1278 = .0909$. This MSE value is enclosed by the 3rd contour in Fig. 14 which leads to a (slightly conservative) 95% confidence band for β_0 of $(-.016, -.006)$. For $r_{trans} = \hat{\alpha}_0 + \hat{\beta}_0 q_a$ we have the extreme values $r_{trans}(q_a = 1.9) = .60$ and $r_{trans}(q_a = 4.2) = .57$. A search over the entire region bounded by the 95% confidence contour yielded $r_{trans}(q_a = 1.9)_{max} = .61$ and $r_{trans}(q_a = 4.2)_{min} = .57$. Thus, although the null-hypothesis $\beta_0 = 0$ was not satisfied, we have established a 95% confidence interval $(.57, .61)$ for r_{trans} for the combined database where q_a varies from 1.9 to 4.2. This small variation in r_{trans} ($r_{trans,max}/r_{trans,min} \simeq 1.1$) clearly contradicts the hypothesis that $r_{trans} \propto 1/q_a$ since we would expect, for our database, that r_{trans} would vary by a factor of $\frac{4.2}{1.9} = 2.2$. We can offer no convincing explanation for this result.

References

- [1] KARDAUN, O.J.W.F., RIEDEL, K.S., MCCARTHY, P.J., LACKNER, K., Max-Planck-Institut für Plasma Physik, Report No. 5/35
- [2] MURAKAMI, M., CALLEN, J.D., BERRY, B.A., Nucl. Fusion **16** (1976) 347.
- [3] MÜLLER, E.R., SÖLDNER, F.X., JANESCHITZ, G., MURMANN, H., FUSSMANN, G., KORNHERR, M., POSCHENRIEDER, W., WAGNER, F., WÜRZ, et al., in Controlled Fusion and Plasma Physics (Proc. 15th Eur. Conf. Dubrovnik, 1988) Europhys. Conf. Abst. Vol. **12B-I**, European Physical Society (1988) 19.
- [4] ARUNASALAM, V.D., BRETZ, N.L., EFTIMION, P.C., et. al., Nuclear Fusion, **30**, (1990) 2111.
- [5] RÖHR, H., STEUER, K.-H., MURMANN H., MEISEL D., Max-Planck-Institut für Plasma Physik, Report No. 3/121 (1987) (also Nucl. Fusion **22** (1982) 1099).
- [6] Mardia, K.V., Kent J.T., Bibby, J.M., Multivariate Analysis Academic Press Inc., London (1979).
- [7] STEUER, K.-H., RÖHR, H., ROBERTS, D.E., et al., in Controlled Fusion and Plasma Physics (Proc. 15th Eur. Conf. Dubrovnik, 1988) Europhys. Conf. Abst. Vol. **12B-I**, European Physical Society (1988) 31.
- [8] KARDAUN, O., THOMSEN, K., CORDEY, J., et al., in Controlled Fusion and Plasma Physics (Proc. 17th Eur. Conf. Amsterdam 1990)

Vol. **14B-I**, European Physical Society (1990) 110.

- [9] PFEIFFER W., WALTZ R., Nucl. Fusion **19** (1979) 51.
- [10] BARTLETT D.V., BICKERTON R.J., BRUSATI M., et al., Nucl. Fusion **28** (1988) 73.
- [11] CHRISTIANSEN, J.P., CALLEN, J.D., CORDEY, J.G., THOMSEN, K., Nucl. Fusion **28** (1988) 817.
- [12] MC CARTHY, P.J., RIEDEL, K.S., KARDAUN, O., MURMANN, H., LACKNER, K., et al., *Scalings and Plasma Profile Parameterisation of ASDEX High Density Ohmic Discharges*, Max-Planck-Institut für Plasmaphysik, Report No. 5/34.
- [13] MERTENS, V., BESSENRODT-WEBERPALS, M., DODEL, G., et al., in: ASDEX Contributions to the 17th European Conference on Controlled Fusion and Plasma Physics, Max-Planck-Institut für Plasma Physik, Report No. 3/164 (1990) 1.
- [14] WAGNER, F., GRUBER, O., BARTIROMO, R. et al., in: ASDEX Contributions to the 12th European Conference on Controlled Fusion and Plasma Physics, Max-Planck-Institut für Plasma Physik, Report No. 3/107 (1985) 16.
- [15] WALTZ, R.E., WONG, S.K., GREENE, J.M., DOMINGUEZ, R.R., Nucl. Fusion **26** (1986) 1729.
- [16] EJIMA, S., PETRIE, T.W., RIVIERE, A.C. et al., Nucl. Fusion **22** (1982) 1627.

- [17] SAS, User's guide: Statistics (6th ed.), SAS Institute Inc., Cary, NC, (1989).
- [18] FREDRICKSON, E.D., MCGUIRE, K.M., GOLDSTON, R.J., et. al., Nuclear Fusion, **27**, p. 1897, (1987).
- [19] ST. JOHN, H., JAHNS, G.I., BURELL, K.H., DEBOO, J.C., Bull. Am. Phys. Soc. (1987) 9.
- [20] POORTEMA, K., On the statistical analysis of growth, PhD thesis, Groningen (1989).
- [21] KARDAUN, O., MC CARTHY, P.J., LACKNER, K., RIEDEL, K., GRUBER, O., in Theory of Fusion Plasmas, Varenna (1987) 435.
- [22] MURMANN H., WAGNER F., et al., in Controlled Fusion and Plasma Physics (Proc. 13th Eur. Conf. Schliersee 1986) Vol. **10C-I**, European Physical Society (1986) 216.
- [23] WEISBERG, S., Technometrics **23** (1981) 27.
- [24] DRAPER, H., SMITH, N., *Applied Regression Analysis*, 2nd ed., Wiley (1981).

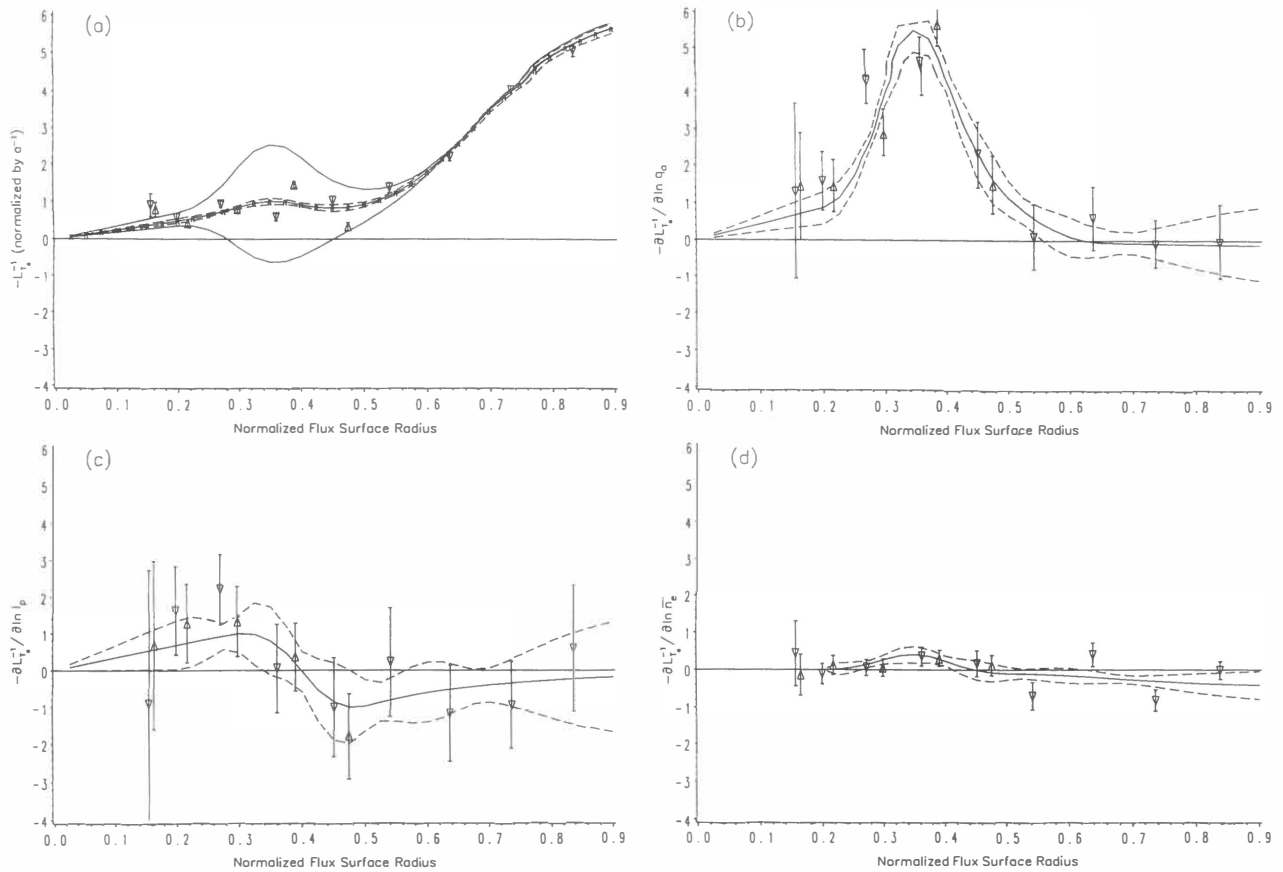


FIG. 5. Reference negative IFOL profiles for the main (high density) database T_e , and parametric dependence profiles for q_a , I_p and \bar{n}_e with local 95% confidence bands. Reference values for discrete (two-channel) IFOLs and the corresponding parametric dependences are also plotted as individual data points. The central solid curve in (a) is the predicted negative IFOL at the reference parameter values $q_a = 2.5$, $I_p = 0.4$ MA, $\bar{n}_e = 0.4 \times 10^{20} \text{ m}^{-3}$. The local 95% confidence bands are plotted as dashed curves. The flattest and steepest predicted negative IFOL profiles in the database (i.e. those for minimum ($q_a = 1.9$) and maximum ($q_a = 3.4$) values of q_a) are plotted as solid curves without confidence bands. The individual data points are predictions for discretely calculated IFOLs (Section 7.1), again evaluated at the reference parameter values and accompanied by 95% confidence bands. (b) Parametric dependence of L_{Te}^{-1} on q_a . The solid curve is the radial profile of the change (in units of $1/\text{minor radius}$) in the negative IFOL per unit change in $\ln q_a$ (see Eq. (11)). The individual data points give similar information on the discrete IFOLs. (c) Parametric dependence of L_{Te}^{-1} on I_p and \bar{n}_e . (d) Parametric dependence of L_{Te}^{-1} on \bar{n}_e .

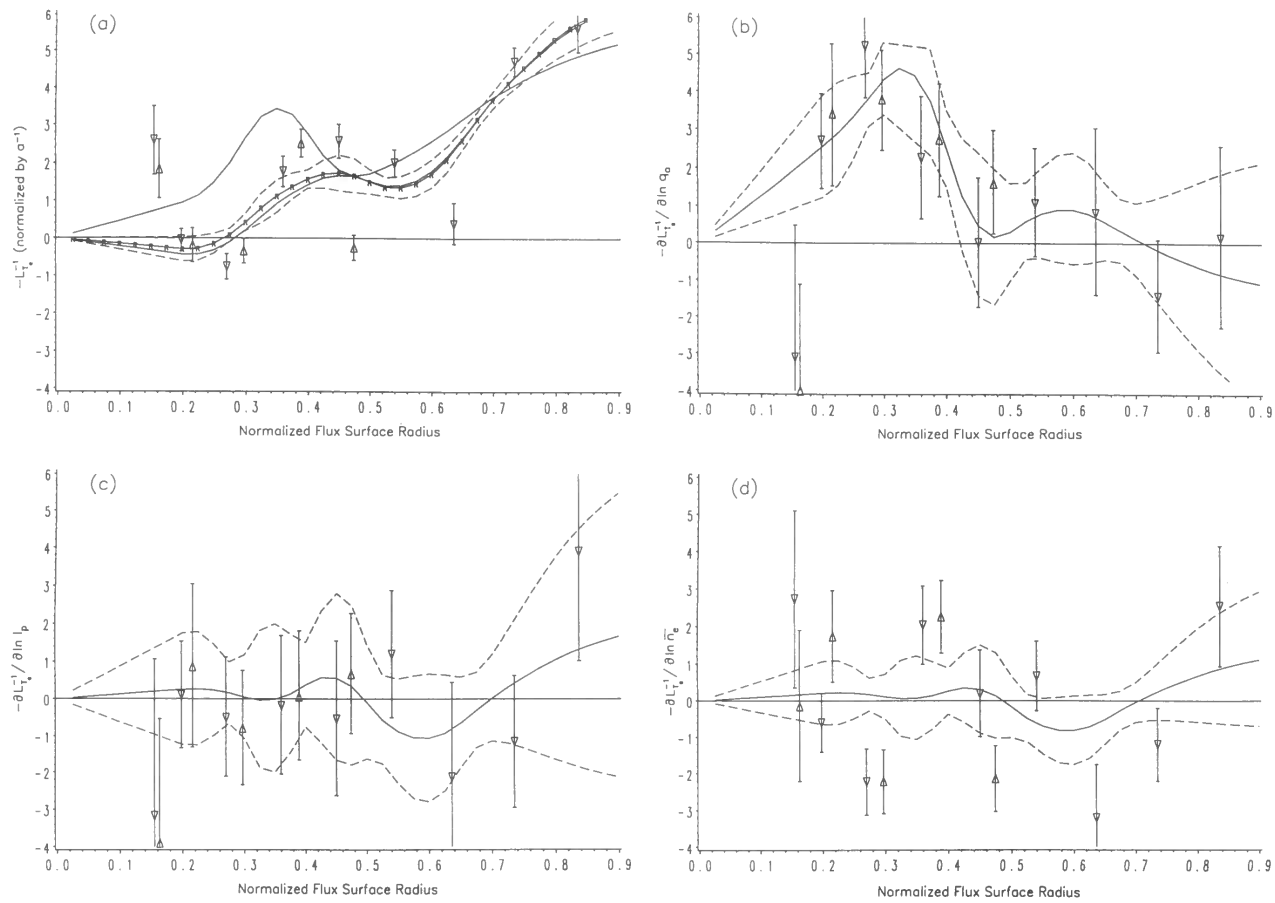


FIG. 6. Reference negative IFOL profiles for the secondary (moderate density) database T_e , and parametric dependence profiles for q_a , I_p and \bar{n}_e .

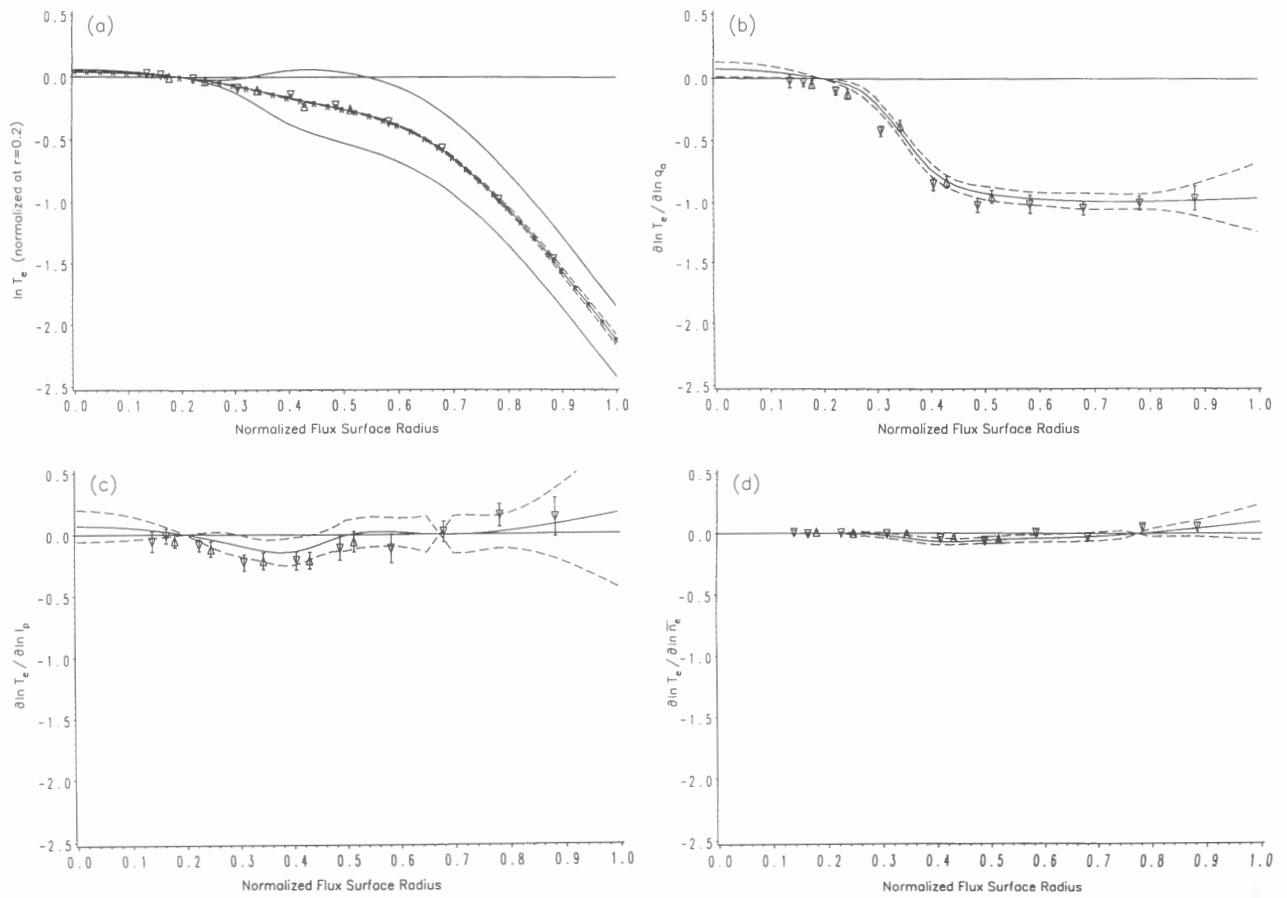


FIG. 7. Reference $\ln T_e$ profiles (normalized at $r = 0.2$) for the main database, and parametric dependence profiles for q_a , I_p and \bar{n}_e .

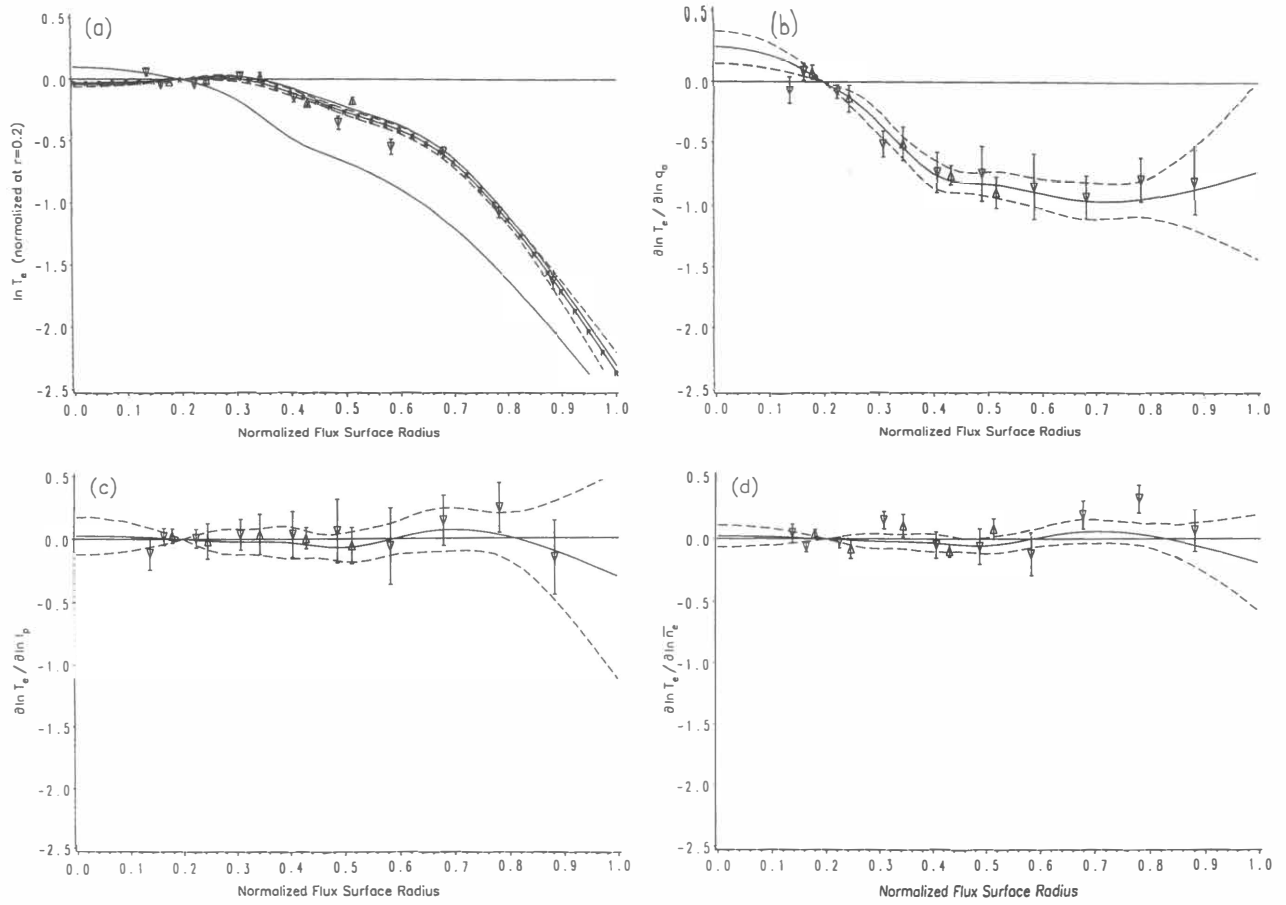


FIG. 8. Reference $\ln T_e$ profiles (normalized at $r = 0.2$) for the secondary database, and parametric dependence profiles for q_a , I_p and \bar{n}_r .

McCARTHY et al.

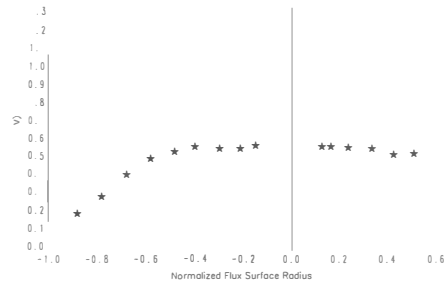


FIG. 9. Sample experimental and predicted temperature profile with global 95% confidence bands from the main database. Parameters: $q_a = 1.94$, $I_p = 0.452$ MA, $\bar{n}_e = 0.704 \times 10^{20} \text{ m}^{-3}$.

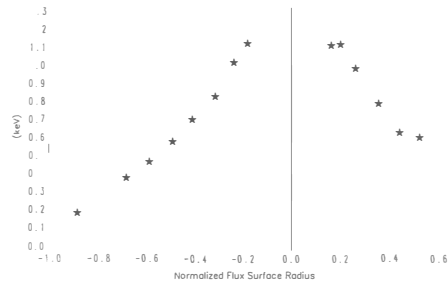


FIG. 10. Sample experimental and predicted temperature profile with global 95% confidence bands from the secondary database. Parameters: $q_a = 4.01$, $I_p = 0.281$ MA, $\bar{n}_e = 0.299 \times 10^{20} \text{ m}^{-3}$.

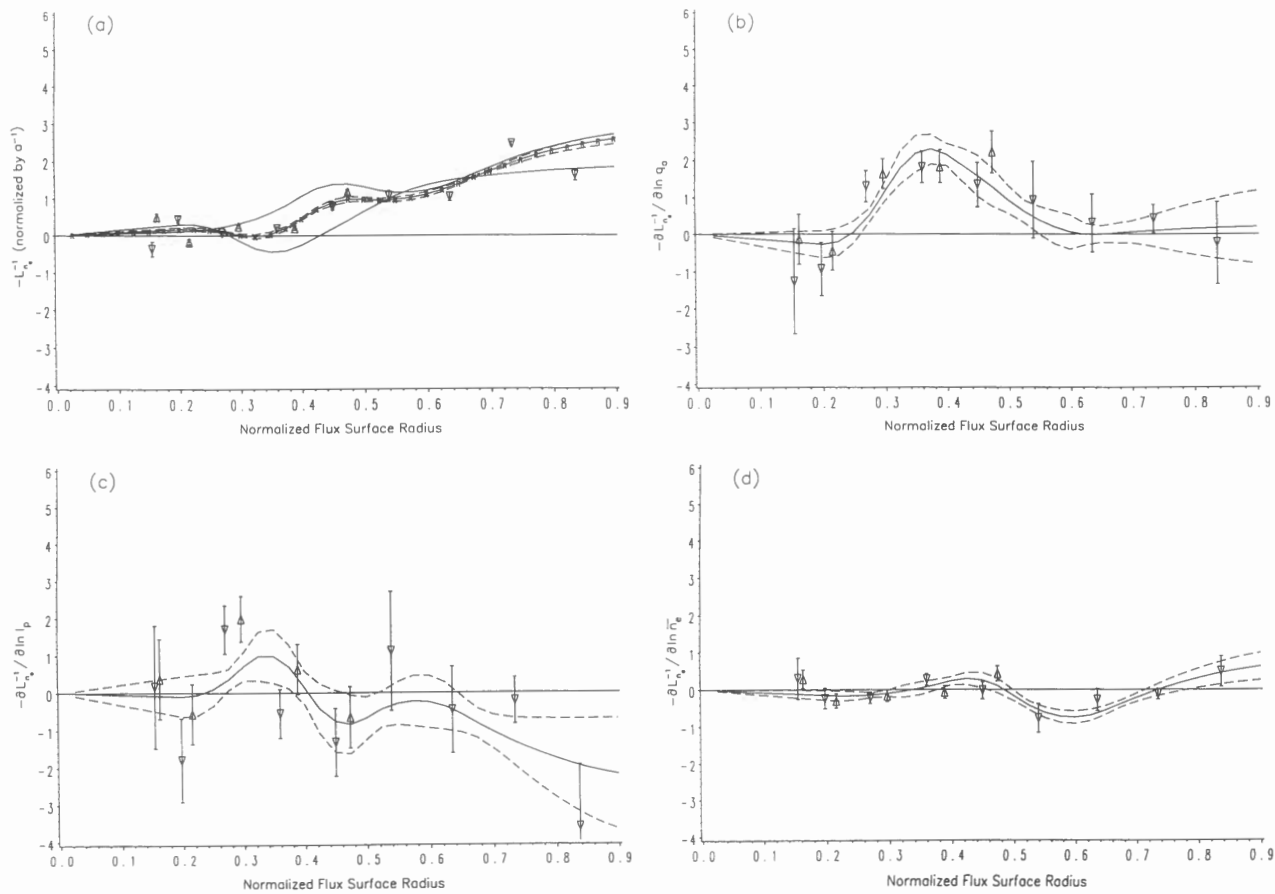


FIG. 11. Reference negative IFOL profiles for the main database n_e , and parametric dependence profiles for q_a , I_p and \bar{n}_e .

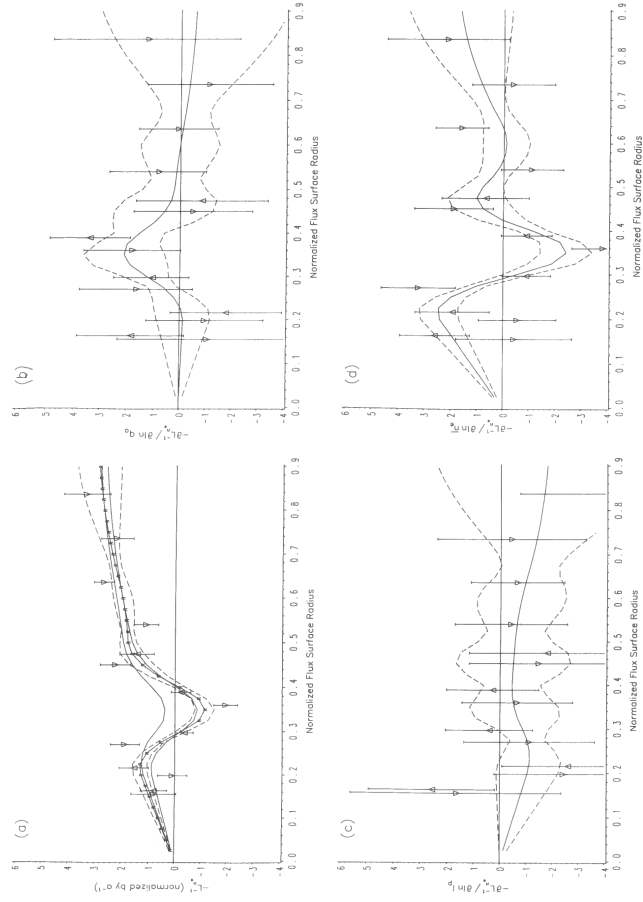


FIG. 12. Reference negative IFOL profiles for the secondary database n_e , and parametric dependence profiles for I_p and n_e .

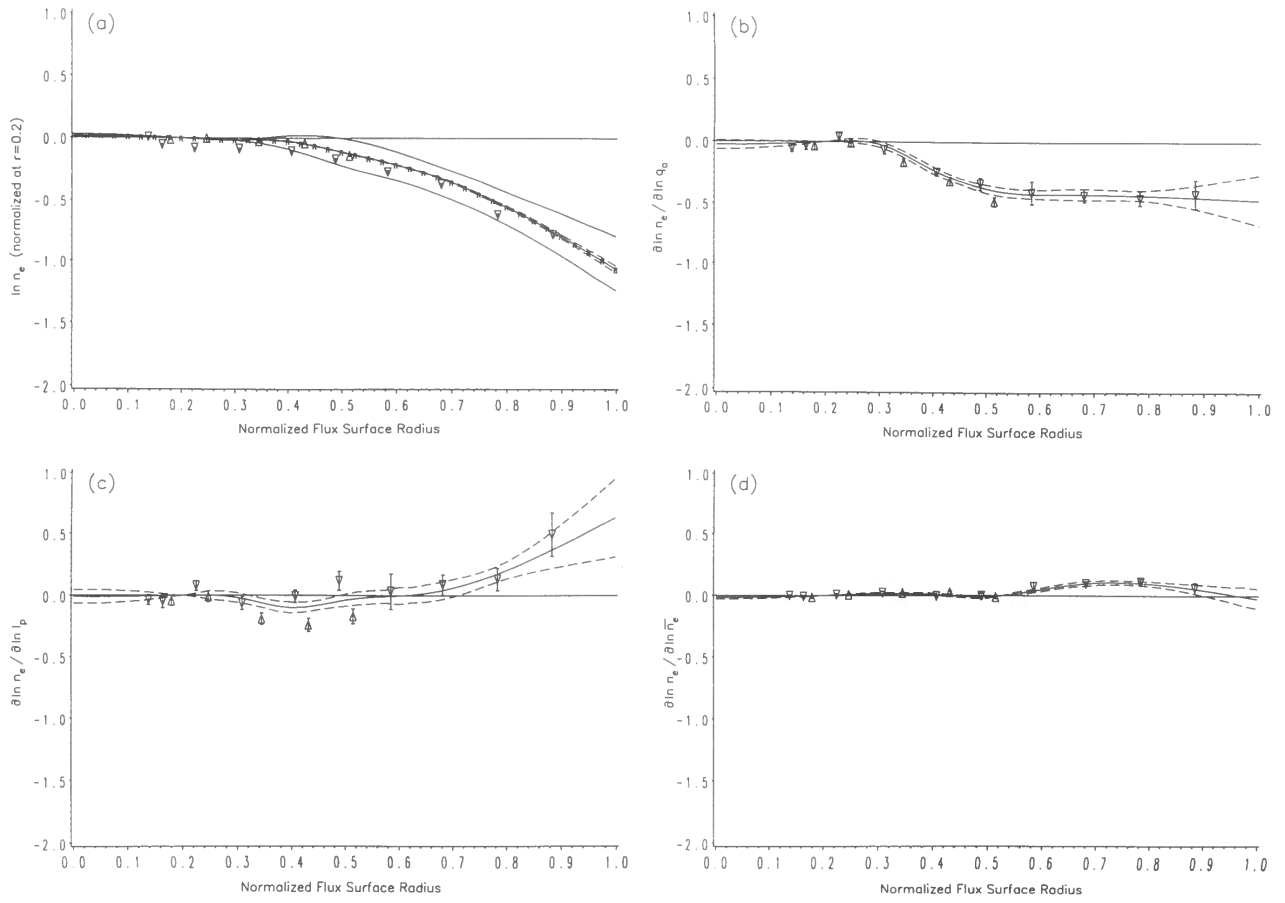


FIG. 13. Reference $\ln n_e$ profiles (normalized at $r = 0.2$) for the main database, and parametric dependence profiles for q_0 , I_p and \bar{n}_e .

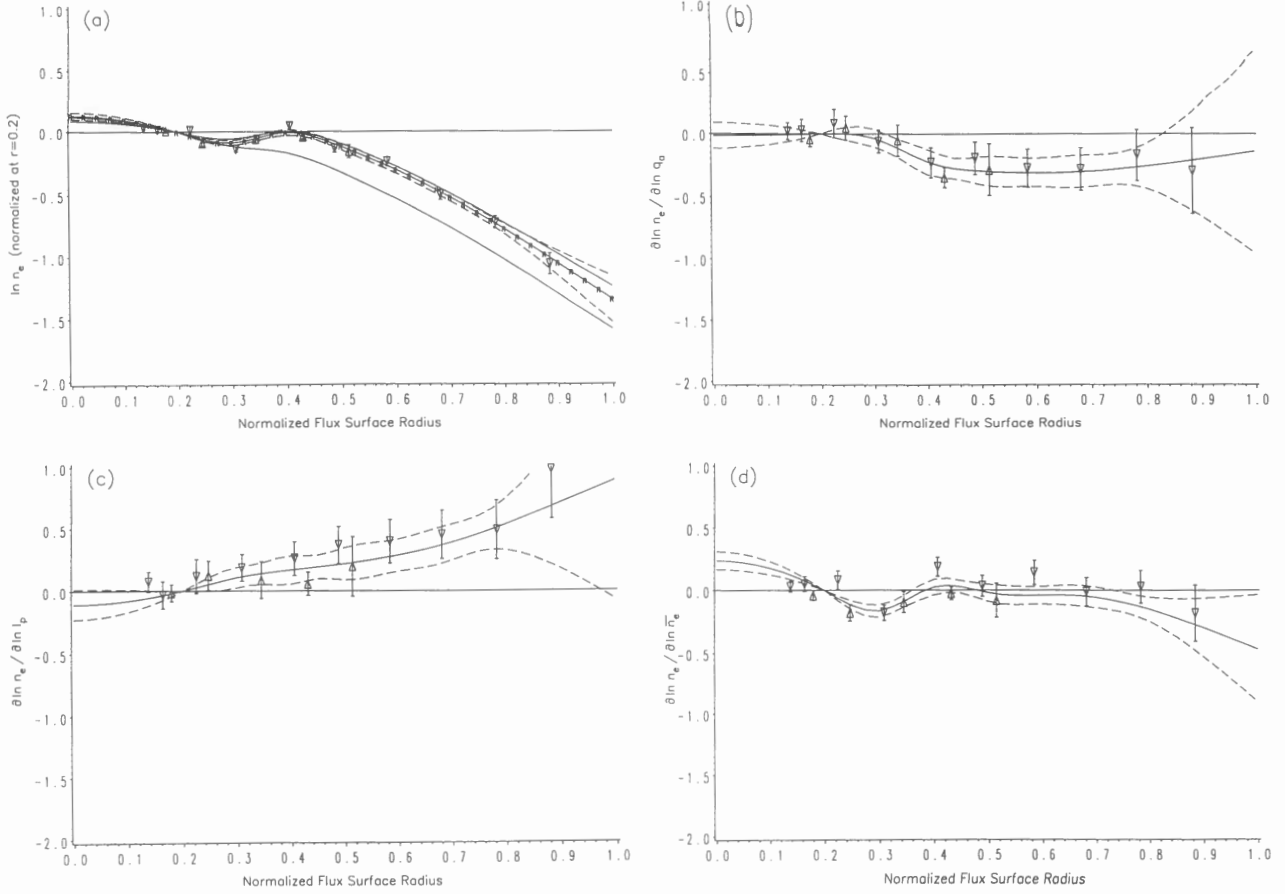


FIG. 14. Reference $\ln n_e$ profiles (normalized at $r = 0.2$) for the secondary database, and parametric dependence profiles for q_a , I_p and \bar{n}_r .

McCARTHY et al.

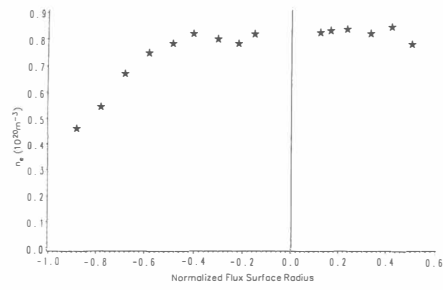


FIG. 15. Sample experimental and predicted density profile with global 95% confidence bands from the main database. Parameters: $q_a = 1.94$, $I_p = 0.452 \text{ MA}$, $\bar{n}_e = 0.704 \times 10^{20} \text{ m}^{-3}$.

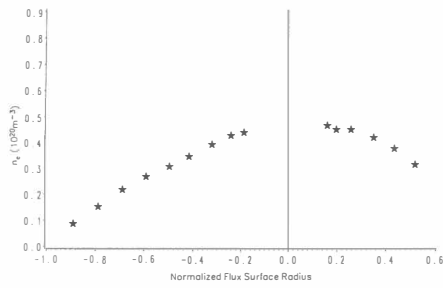


FIG. 16. Sample experimental and predicted density profile with global 95% confidence bands from the secondary database. Parameters: $q_a = 4.01$, $I_p = 0.281 \text{ MA}$, $\bar{n}_e = 0.299 \times 10^{20} \text{ m}^{-3}$.

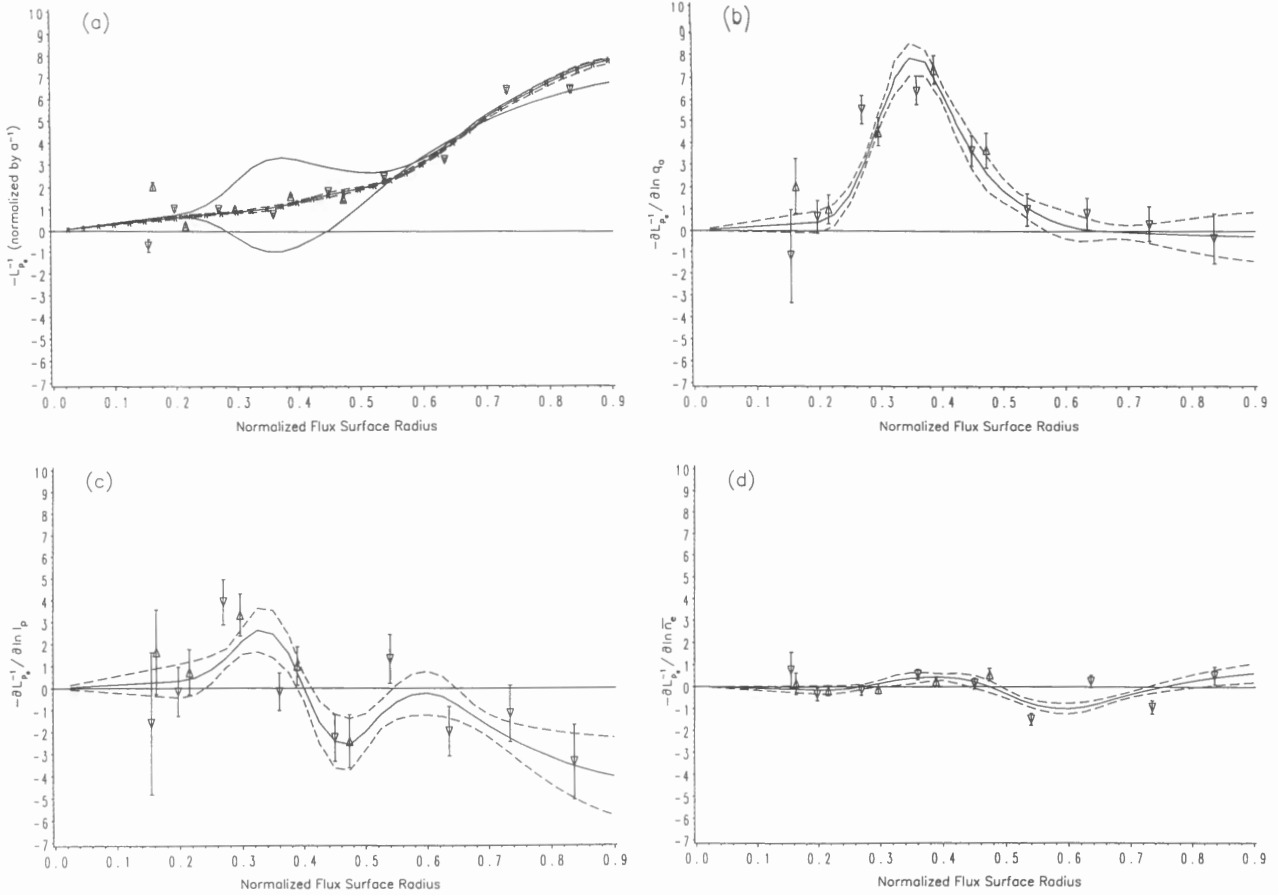


FIG. 17. Reference negative IFOL profiles for the main database p_e , and parametric dependence profiles for q_e , I_p and \bar{n}_e .

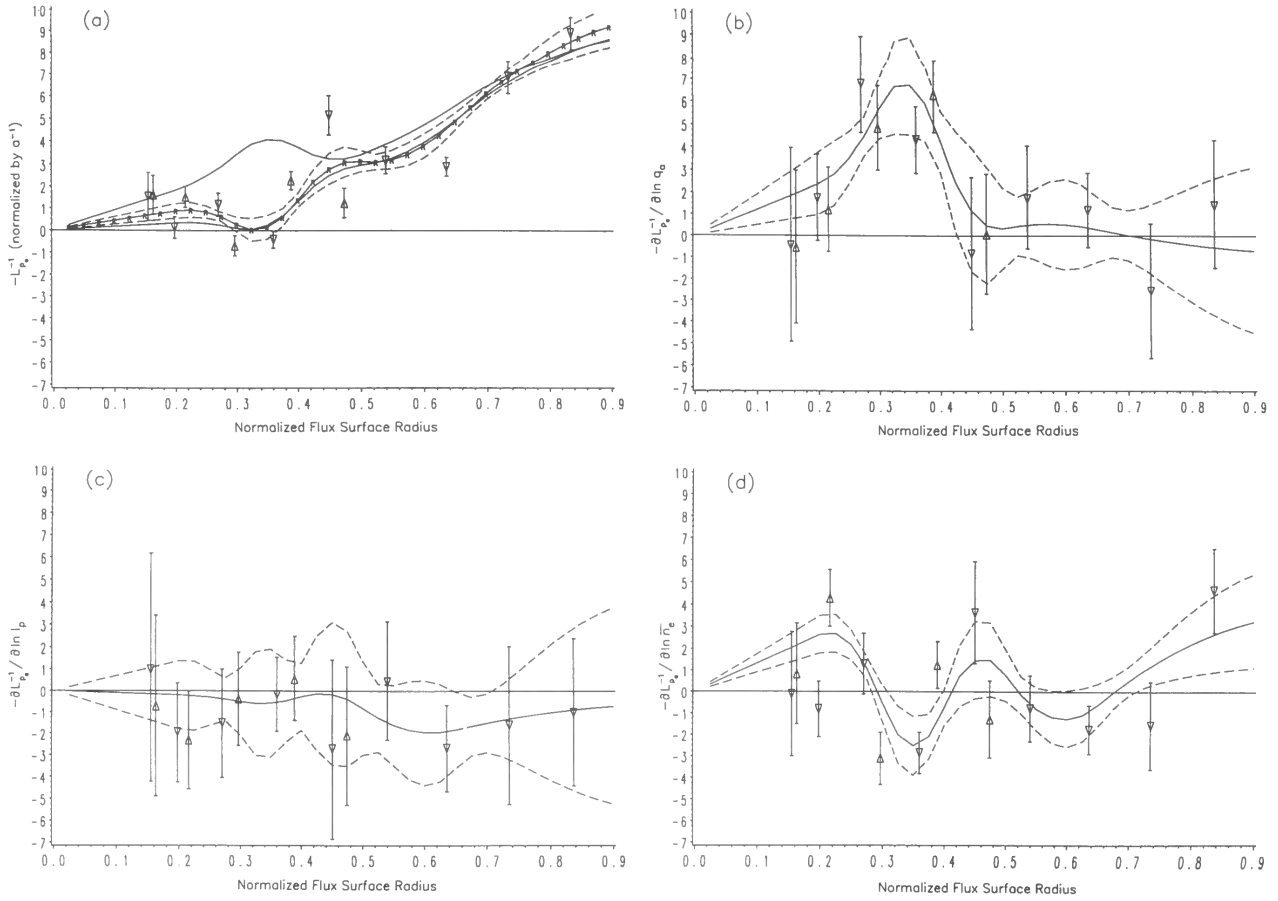


FIG. 18. Reference negative IFOL profiles for the secondary database p_e , and parametric dependence profiles for q_a , I_p and \bar{n}_e .

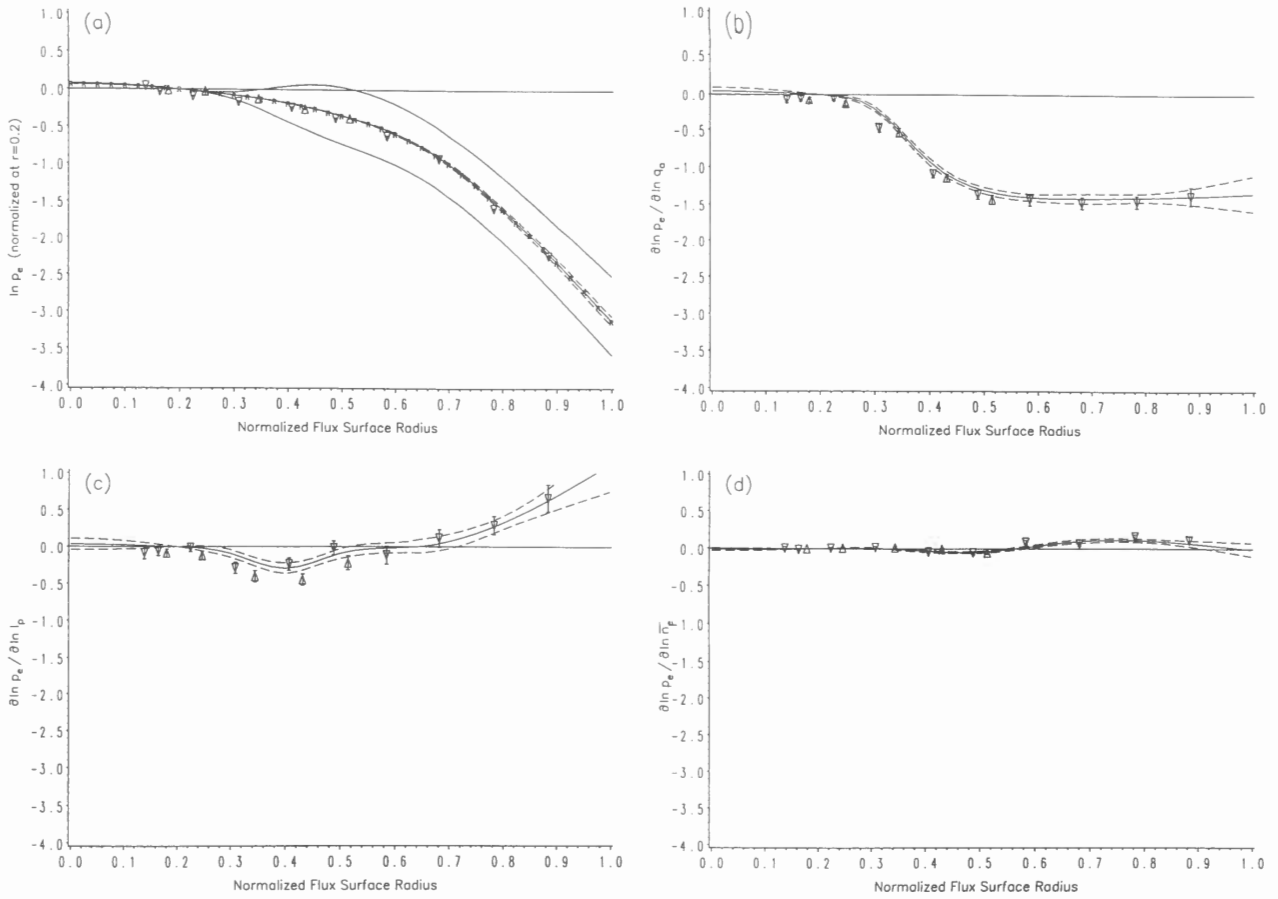


FIG. 19. Reference $\ln p_e$ profiles (normalized at $r = 0.2$) for the main database, and parametric dependence profiles for q_e , I_p and \bar{n}_e .

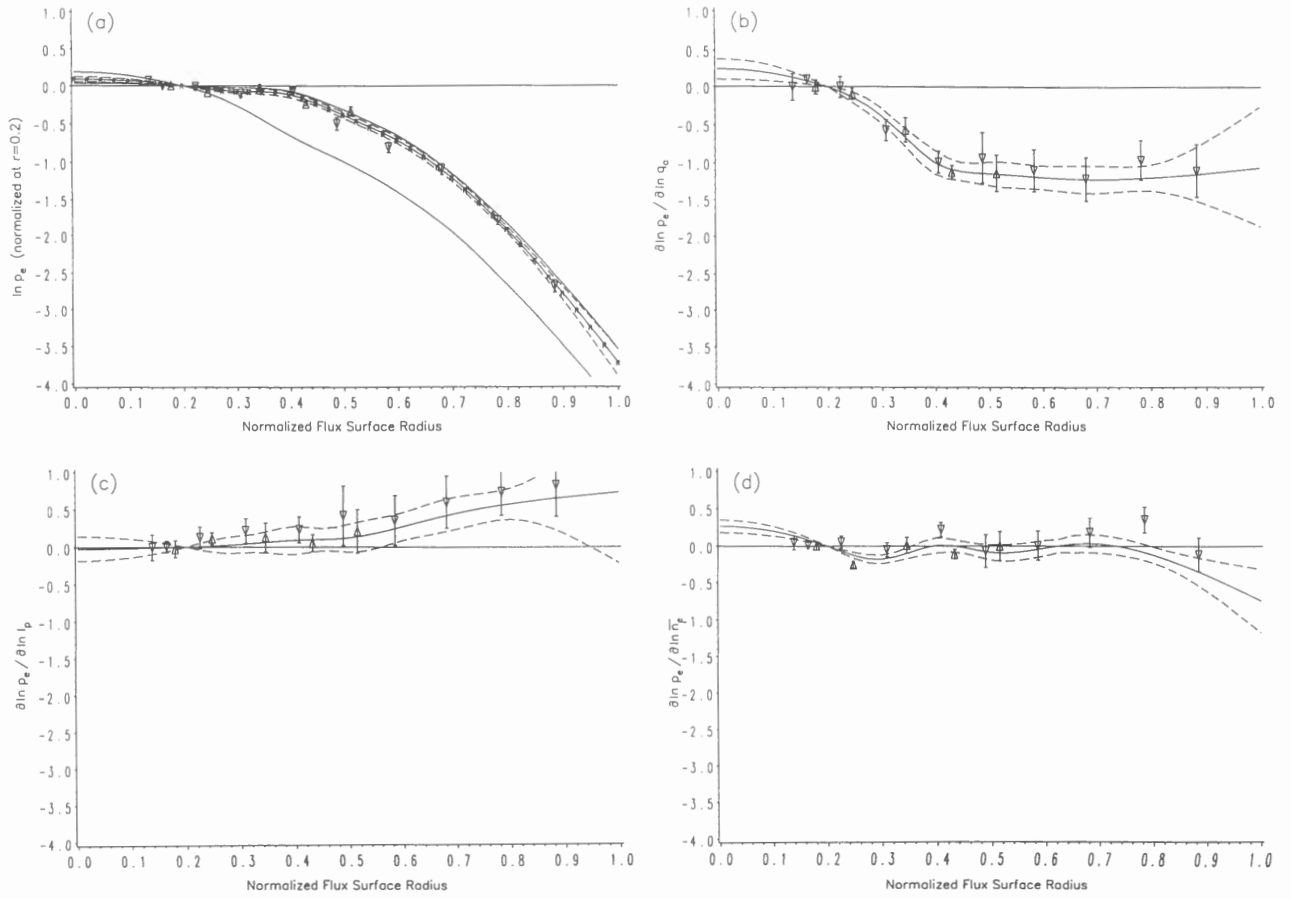


FIG. 20. Reference $\ln p_e$ profiles (normalized at $r = 0.2$) for the secondary database, and parametric dependence profiles for q_0 , I_0 and \bar{n}_r .